Computers & Geosciences 152 (2021) 104774

Contents lists available at ScienceDirect

Computers and Geosciences

journal homepage: www.elsevier.com/locate/cageo

Research paper

A locally conservative mixed finite element framework for coupled hydro-mechanical–chemical processes in heterogeneous porous media ☆

T. Kadeethum [a,b], S. Lee [c], F. Ballarin [d,e], J. Choo [f], H.M. Nick [a,g,*]

[a] Danish Hydrocarbon Research and Technology Centre, Technical University of Denmark, Denmark
[b] Sibley School of Mechanical and Aerospace Engineering, Cornell University, NY, USA
[c] Department of Mathematics, Florida State University, FL, USA
[d] mathLab, Mathematics Area, SISSA, Trieste, Italy
[e] Department of Mathematics and Physics, Catholic University of the Sacred Heart, Brescia, Italy
[f] Department of Civil Engineering, The University of Hong Kong, Hong Kong
[g] Department of Civil Engineering, Delft University of Technology, The Netherlands

ARTICLE INFO

Keywords:
Hydro-mechanical–chemical coupling
Poroelasticity
Reactive flow
Mixed finite element method
Enriched Galerkin method
Local conservation

ABSTRACT

This paper presents a mixed finite element framework for coupled hydro-mechanical–chemical processes in heterogeneous porous media. The framework combines two types of locally conservative discretization schemes: (1) an enriched Galerkin method for reactive flow, and (2) a three-field mixed finite element method for coupled fluid flow and solid deformation. This combination ensures local mass conservation, which is critical to flow and transport in heterogeneous porous media, with a relatively affordable computational cost. A particular class of the framework is constructed for calcite precipitation/dissolution reactions, incorporating their nonlinear effects on the fluid viscosity and solid deformation. Linearization schemes and algorithms for solving the nonlinear algebraic system are also presented. Through numerical examples of various complexity, we demonstrate that the proposed framework is a robust and efficient computational method for simulation of reactive flow and transport in deformable porous media, even when the material properties are strongly heterogeneous and anisotropic.

1. Introduction

Hydro-mechanical–chemical (HMC) processes in porous media, in which fluid flow, solid deformation, and chemical reactions are tightly coupled, appear in a variety of problems ranging from groundwater and contaminant hydrology to subsurface energy production (Nick et al., 2013; Hu and Hueckel, 2013; Pandey et al., 2014; Pandey and Chaudhuri, 2017; Nick et al., 2015; Choo and Sun, 2018; Tran and Jha, 2020). The porous media in these problems are often strongly heterogeneous, not only because they are naturally heterogeneous materials (e.g. rocks and soils) but also because HMC interactions strengthen the material heterogeneity. For instance, change in pore pressure perturbs effective stress in the solid matrix, which can, in turn, alter the conductivity and storability of the porous medium (Chen, 2007; Du and Wong, 2007; Abou-Kassem et al., 2013; Kadeethum et al., 2018, 2019b, 2020c; Nejati et al., 2019). Similarly, chemical processes can result in the precipitation or dissolution of solid minerals, which decreases or increases the pore volume, respectively, and thus, the conductivity (Salimzadeh et al., 2019; Pandey et al., 2014; Pandey and Chaudhuri, 2017; Rutqvist, 2017; Ahkami et al., 2020; Choo and Sun, 2018). Therefore, accurate numerical modeling of coupled HMC problems requires a computational method that can robustly handle strong heterogeneity in porous media.

Nevertheless, it remains challenging to simulate coupled HMC processes in porous media in a robust and efficient manner, especially when the material properties are highly heterogeneous and/or anisotropic. Because HMC problems involve transport phenomena in heterogeneous porous media, the numerical method for these problems must ensure local (element-wise) conservation (Riviere, 2008; Lee et al., 2016). The most practical method featuring local mass conservation may be the finite volume method with a standard two-point flux approximation scheme. However, this standard finite volume method requires the grid to be aligned with the principal directions of the permeability/diffusivity tensors (Lipnikov et al., 2009; Choo and Sun, 2018), which inhibits the use of an unstructured grid when

☆ This research has been awarded the funding from the 2019 Computers & Geosciences Research grant.
* Corresponding author at: Department of Civil Engineering, Delft University of Technology, The Netherlands.
E-mail addresses: tk658@cornell.edu (T. Kadeethum), lee@math.fsu.edu (S. Lee), francesco.ballarin@unicatt.it (F. Ballarin), jchoo@hku.hk (J. Choo), h.m.nick@tudelft.nl (H.M. Nick).

https://doi.org/10.1016/j.cageo.2021.104774
Received 17 June 2020; Received in revised form 31 March 2021; Accepted 31 March 2021
Available online 9 April 2021

the permeability/diffusivity tensors are anisotropic. Multi-point flux-approximation methods have been developed to tackle this issue (Aavatsmark, 2002), but their implementation is often complicated and onerous (Choo, 2018). Discontinuous Galerkin (DG) methods offer an elegant way to handle arbitrarily anisotropic tensor conductivity/diffusivity. However, their computational cost is often impractical as a result of the proliferation of the degrees of freedom.

In this paper, we present a new framework for computational modeling of coupled HMC processes in porous media, which efficiently provides local mass conservation even when the material properties are strongly heterogeneous and anisotropic. The proposed framework combines two types of discretization methods: (1) an enriched Galerkin (EG) method for reactive flow and transport, and (2) a three-field mixed finite element method for coupled hydro-mechanical processes. The EG method, which has recently been developed and advanced in the literature (Sun and Liu, 2009; Lee et al., 2016; Lee and Wheeler, 2018; Choo and Lee, 2018; Choo, 2018, 2019; Kadeethum et al., 2020a, 2021b; Rupp and Lee, 2020; Choi and Lee, 2020), augments a piecewise constant function to the continuous Galerkin (CG) function space. This method uses the same interior penalty type form as the DG method, but it requires a substantially fewer number of degrees of freedom than the DG method. Thus the EG method can provide locally conservative solutions to the reactive flow system regardless of the grid-conductivity alignment. For the hydro-mechanical sub-system of the HMC problem, we use a three-field mixed finite element formulation (Phillips and Wheeler, 2007a,b; Haga et al., 2012), which provides locally conservative, high-order solutions to the fluid velocity field. Specifically, we employ the Lagrange finite elements for approximating the displacement field, the Brezzi–Douglas–Marini (BDM) element for the fluid velocity field, and the piecewise constant element for the fluid pressure field. It is noted that this combination of elements is our personal choice, and one may use another combination for the same three primary fields as in Ferronato et al. (2010), Jha and Juanes (2007) and Haga et al. (2012).

The purpose of this work is to develop an accurate numerical method for tackling coupled HMC processes in heterogeneous porous media, with a practically affordable computational cost. Our specific objectives can be summarized as follows:

1. To formulate a robust numerical approximation scheme for coupled HMC processes in heterogeneous porous media, employing a combination of locally conservative finite element methods.
2. To reduce the computational cost for solving an advection–diffusion–reaction equation by using the EG method, which requires approximately two and three times fewer degrees of freedom than the DG method for 2D and 3D geometries, respectively (Kadeethum et al., 2020b).
3. To demonstrate the performance and capabilities of the proposed framework for modeling tightly coupled HMC problems with homogeneous to heterogeneous, isotropic to anisotropic permeability fields with local conservation.

The rest of the paper is organized as follows. Section 2 describes the governing equations of coupled HMC processes. Section 3 explains the discretization methods, linearization techniques, and solution algorithms of the proposed framework. Section 4 presents several numerical examples of various complexity and discusses key points found in this paper. Section 5 concludes the work.

2. Governing equations

This section briefly describes all the equations used in this study, namely poroelasticity and advection–diffusion–reaction equations.

Let $\Omega \subset \mathbb{R}^d$ ($d \in \{1,2,3\}$) denote the computational domain and $\partial\Omega$ denote the boundary. The time domain is denoted by $\mathbb{T} = (0, \mathrm{T}]$ with $\mathrm{T} > 0$. Primary variables used in this paper are $\boldsymbol{q}(\cdot,t) : \Omega \times \mathbb{T} \to \mathbb{R}^d$, which is a vector-valued Darcy velocity (m/s), $p(\cdot,t) : \Omega \times \mathbb{T} \to \mathbb{R}$, which is a scalar-valued fluid pressure (Pa), $\boldsymbol{u}(\cdot,t) : \Omega \times \mathbb{T} \to \mathbb{R}^d$, which is a vector-valued displacement (m), $c_i : \Omega \times \mathbb{T} \to \mathbb{R}$, which is the ith component of chemical concentration (mmol/m^3).

2.1. Poroelasticity

To begin, we adopt Biot's poroelasticity theory for coupled hydro-mechanical processes in porous media (Biot, 1941; Biot and Willis, 1957). Although poroelasticity may oversimplify deformations in soft porous materials such as soils (Choo et al., 2016; Borja and Choo, 2016; MacMinn et al., 2016; Zhao and Choo, 2020; Kadeethum et al., 2021a), it would be reasonably good for stiff materials such as rocks, which is the focus of this work. The poroelasticity theory provides two coupled governing equations, namely linear momentum and mass balance equations. Under quasi-static conditions, the linear momentum balance equation can be written as

$$\nabla \cdot \boldsymbol{\sigma}(\boldsymbol{u}, p) + \boldsymbol{f} = \boldsymbol{0}, \tag{1}$$

where $\boldsymbol{f}$ is the body force term defined as $\rho\phi\mathbf{g} + \rho_s(1-\phi)\mathbf{g}$, where ρ is the fluid density, ρ_s is the solid density, ϕ is the porosity, $\mathbf{g}$ is the gravitational acceleration vector. The gravitational force will be neglected in this study, but the body force term will be kept in the succeeding formulations for a more general case. Further, $\boldsymbol{\sigma}$ is the total stress tensor, which may be related to the effective stress tensor $\boldsymbol{\sigma}'$ and the pore pressure p as

$$\boldsymbol{\sigma}(\boldsymbol{u}, p) = \boldsymbol{\sigma}'(\boldsymbol{u}) - \alpha p \mathbf{I}. \tag{2}$$

Here, $\mathbf{I}$ is the second-order identity tensor, and α is the Biot coefficient defined as (Jaeger et al., 2009):

$$\alpha = 1 - \frac{K}{K_s}, \tag{3}$$

with K and K_s being the bulk moduli of the solid matrix and the solid grain, respectively. According to linear elasticity, the effective stress tensor has a constitutive relationship with the displacement vector, which can be written as

$$\boldsymbol{\sigma}'(\boldsymbol{u}) = \lambda_l \operatorname{tr}(\boldsymbol{\varepsilon}(\boldsymbol{u}))\mathbf{I} + 2\mu_l \boldsymbol{\varepsilon}(\boldsymbol{u}). \tag{4}$$

Here, $\boldsymbol{\varepsilon}$ is the infinitesimal strain tensor, defined as

$$\boldsymbol{\varepsilon}(\boldsymbol{u}) := \frac{1}{2}\left(\nabla \boldsymbol{u} + (\nabla \boldsymbol{u})^{\mathrm{T}}\right), \tag{5}$$

and λ_l and μ_l are the Lamé constants, which are related to the bulk modulus and the Poisson ratio ν of the solid matrix as

$$\lambda_l = \frac{3K\nu}{1+\nu}, \text{ and } \mu_l = \frac{3K(1-2\nu)}{2(1+\nu)}. \tag{6}$$

For this solid deformation problem, the domain boundary $\partial\Omega$ is assumed to be suitably decomposed into displacement and traction boundaries, $\partial\Omega_u$ and $\partial\Omega_t$, respectively. Then the linear momentum balance equation is supplemented by the boundary and initial conditions as:

$$\begin{aligned} \nabla \cdot \boldsymbol{\sigma}'(\boldsymbol{u}) - \alpha \nabla \cdot (p\mathbf{I}) + \boldsymbol{f} &= \boldsymbol{0} \quad \text{in} \quad \Omega \times \mathbb{T}, \\ \boldsymbol{u} &= \boldsymbol{u}_D \quad \text{on} \quad \partial\Omega_u \times \mathbb{T}, \\ \boldsymbol{\sigma}(\boldsymbol{u}) \cdot \mathbf{n} &= \boldsymbol{t}_D \quad \text{on} \quad \partial\Omega_t \times \mathbb{T}, \\ \boldsymbol{u} &= \boldsymbol{u}_0 \quad \text{in} \quad \Omega \text{ at } t = 0, \end{aligned} \tag{7}$$

where $\boldsymbol{u}_D$ and $\boldsymbol{t}_D$ are prescribed displacement and traction values at the boundaries, respectively, and $\mathbf{n}$ is the unit normal vector to the boundary.

Next, the mass balance equation is given as (Coussy, 2004; Kim et al., 2011; Pandey and Chaudhuri, 2017; Salimzadeh and Nick, 2019):

$$\frac{1}{M}\frac{\partial p}{\partial t} + \alpha \frac{\partial \varepsilon_v}{\partial t} + \frac{\partial \phi_c}{\partial t} + \nabla \cdot \boldsymbol{q} = g \text{ in } \Omega \times \mathbb{T}, \tag{8}$$

where

$$\frac{1}{M} = \left(\phi_0 c_f + \frac{\alpha - \phi_0}{K_s}\right) \tag{9}$$

is the Biot modulus. Here, c_f is the fluid compressibility, ϕ_0 is the initial porosity, $\varepsilon_v := \mathrm{tr}(\boldsymbol{\varepsilon}) = \nabla \cdot \boldsymbol{u}$ is the volumetric strain, and g is a sink/source term. Because we will introduce chemical effects later on, we have added $\frac{\partial \phi_c}{\partial t}$ to the standard poroelasticity equation (Chaudhuri et al., 2013; Pandey et al., 2014; Pandey and Chaudhuri, 2017; Salimzadeh and Nick, 2019). This term will be discussed again after introducing chemical effects. Also, $\boldsymbol{q}$ is the superficial velocity vector, which is given by Darcy's law as

$$\boldsymbol{q} = -\frac{\boldsymbol{k}(\phi)}{\mu(c_i)}(\nabla p - \rho \mathbf{g}). \tag{10}$$

Note that here the fluid viscosity μ is considered a function of concentration c_i. Again, the gravitational force, $\rho\mathbf{g}$, will be neglected in this work, without loss of generality. In addition, $\boldsymbol{k}(\phi)$ is the matrix permeability tensor defined as

$$\boldsymbol{k} := \begin{cases} k_{mult}(\phi) \begin{bmatrix} k^{xx} & k^{xy} & k^{xz} \\ k^{yx} & k^{yy} & k^{yz} \\ k^{zx} & k^{zy} & k^{zz} \end{bmatrix} & \text{if } d = 3, \\ k_{mult}(\phi) \begin{bmatrix} k^{xx} & k^{xy} \\ k^{yx} & k^{yy} \end{bmatrix} & \text{if } d = 2, \\ k_{mult}(\phi)\, k & \text{if } d = 1, \end{cases} \tag{11}$$

The k^{xx}, k^{yy}, and k^{zz} represent the matrix permeability in x-, y-, and z-direction, respectively. The $k_{mult}(\phi)$ is a multiplier used to update $\boldsymbol{k}$ when ϕ is altered, which will be described later.

For the fluid flow problem, the domain boundary $\partial\Omega$ is also suitably decomposed into the pressure and flux boundaries, $\partial\Omega_p$ and $\partial\Omega_q$, respectively. In what follows, we apply the fixed stress split scheme (Kim et al., 2011; Mikelic and Wheeler, 2013), assuming $(\sigma_v - \sigma_{v,0}) + \alpha\,(p - p_0) = K\varepsilon_v$. Then we write the fluid flow problem with boundary and initial conditions as

$$\begin{aligned} \left(\frac{1}{M} + \frac{\alpha^2}{K}\right)\frac{\partial p}{\partial t} + \frac{\alpha}{K}\frac{\partial \sigma_v}{\partial t} + \frac{\partial \phi_c}{\partial t} + \nabla \cdot \boldsymbol{q} = g \quad &\text{in} \quad \Omega \times \mathbb{T}, \\ p = p_D \quad &\text{on} \quad \partial\Omega_p \times \mathbb{T}, \\ \boldsymbol{q} \cdot \mathbf{n} = q_D \quad &\text{on} \quad \partial\Omega_q \times \mathbb{T}, \\ p = p_0 \quad &\text{in} \quad \Omega \text{ at } t = 0, \end{aligned} \tag{12}$$

where $\sigma_v := \frac{1}{3}\mathrm{tr}(\boldsymbol{\sigma})$ is the volumetric stress, and p_D and q_D are the given boundary pressure and flux, respectively.

2.2. Reactive flow

An advection–diffusion–reaction system for N_c number of the miscible species is given by the following equations. For all $i = 1, \ldots, N_c$,

$$\frac{\partial}{\partial t}(\phi c_i) + \nabla \cdot \eta(\boldsymbol{q}, c_i) = q_i(c_i), \quad \text{in } \Omega \times \mathbb{T}, \tag{13}$$

where $q_i(c_i)$ is a reaction term coupled with sink/source for each component, and the mass flux $\eta(\boldsymbol{q}, c_i)$ is defined as

$$\eta(\boldsymbol{q}, c_i) := \boldsymbol{q} c_i - \boldsymbol{D}_{e,i}(\phi)\nabla c_i. \tag{14}$$

Here $\boldsymbol{D}_{e,i}(\phi)$ is the effective diffusion coefficient tensor defined as

$$\boldsymbol{D}_{e,i} := \frac{\phi}{\tau}\boldsymbol{D}_i, \tag{15}$$

where $\tau = \phi^{-\frac{1}{2}}$ (Tjaden et al., 2016; Mu et al., 2008) and $\boldsymbol{D}_i$ is the given diffusion coefficient tensor. The boundary for the advection–diffusion–reaction system is decomposed into inflow and outflow boundaries, denoted by $\partial\Omega_{\text{in}}$ and $\partial\Omega_{\text{out}}$, respectively, which are defined as

$$\partial\Omega_{\text{in}} := \{\boldsymbol{x} \in \partial\Omega : \boldsymbol{q} \cdot \mathbf{n} < 0\} \quad \text{and} \quad \partial\Omega_{\text{out}} := \{\boldsymbol{x} \in \partial\Omega : \boldsymbol{q} \cdot \mathbf{n} \geq 0\}. \tag{16}$$

In what follows, we specialize the model to calcite precipitation and dissolution reactions, which requires us to solve a calcite–carbonic acid system. In general, the system requires eight transport equations to solve the concentration values of the following main species/ions: $\{H^+, Ca^{2+}, CaHCO_3^+, OH^-, CO_3^{2-}, HCO_3^-, H_2CO_3^*, CaCO_3^*(Aq)\}$ (Chaudhuri et al., 2013; Pandey et al., 2014; Raoof et al., 2013; Morel and Hering, 1993). For simplicity, in this paper we consider a reduced system based on the empirical relationship presented in Chaudhuri et al. (2013), Pandey et al. (2014) and Pandey and Chaudhuri (2017), in which N_c decreases to 1. Thus, letting $c := c_1$, we write the advection–diffusion–reaction system with its boundary and initial conditions as follows:

$$\begin{aligned} \frac{\partial}{\partial t}(\phi c) + \nabla \cdot (\boldsymbol{q} c) - \nabla \cdot \left(\boldsymbol{D}_e(\phi)\nabla c\right) = q \quad &\text{in} \quad \Omega \times (0, \mathbb{T}], \\ \eta(\boldsymbol{q}, c) \cdot \mathbf{n} = c_{in}\boldsymbol{q} \cdot \mathbf{n} \quad &\text{on} \quad \partial\Omega_{\text{in}} \times (0, \mathbb{T}], \\ \boldsymbol{D}_e(\phi)\nabla c \cdot \mathbf{n} = 0 \quad &\text{on} \quad \partial\Omega_{\text{out}} \times (0, \mathbb{T}], \\ c = c_0 \quad &\text{in} \quad \Omega \text{ at } t = 0, \end{aligned} \tag{17}$$

where c_{in} is the inflow concentration, c_0 is the initial concentration, and q represents a source term reflecting the calcite dissolution/precipitation reactions. For this term, here we adopt the term in Chaudhuri et al. (2013), Pandey et al. (2014) and Pandey and Chaudhuri (2017), given by

$$q = R_c A_s, \tag{18}$$

where A_s is the specific surface area, and R_c is the reaction rate calculated as

$$R_c = \begin{cases} 10^r, & \text{for } \widetilde{c} > 0, \\ -10^r, & \text{for } \widetilde{c} < 0, \\ 0.0, & \text{for } \widetilde{c} = 0, \end{cases} \tag{19}$$

with

$$\widetilde{c} = \frac{(c_{eq} - c)}{c_{eq}}, \tag{20}$$

$$r = a_0 + a_1\tau + a_2 \log|\widetilde{c}| + a_3\tau^2 + a_4\tau \log|\widetilde{c}| + a_5(\log|\widetilde{c}|)^2, \tag{21}$$

and

$$\begin{aligned} c_{eq} = {} & 1.417 \times 10^{-3} + 3.823 \times 10^{-6}p - 4.313 \times 10^{-7}\tau \\ & - 2.148 \times 10^{-8}p^2 + 4.304 \times 10^{-8}p\tau - 7.117 \times 10^{-8}\tau^2. \end{aligned} \tag{22}$$

Here, τ is the medium temperature, and a_0, a_1, a_2, a_3, a_4, and a_5 are defined in Table 1.

Before closing this section, we describe physical properties that are coupled with primary variables, $\boldsymbol{u}$, $\boldsymbol{q}$, p, and c. The porosity change due to solid deformation may be expressed as (Biot, 1941; Dana et al., 2018; Dana and Wheeler, 2018):

$$\phi_m = \phi_0 + (\alpha - \phi_0)\left(\epsilon_v - \epsilon_{v_0}\right) + \frac{(\alpha - \phi_0)(1 - \alpha)}{K}(p - p_0), \tag{23}$$

where ϵ_{v_0} is the initial volumetric strain. The porosity alteration due to calcite dissolution/precipitation is calculated as

$$\Gamma(\boldsymbol{u}, c) = \frac{\partial \phi_c}{\partial t} = \frac{R_c A_s}{\rho_s \omega}, \tag{24}$$

where $\rho_s\omega$ is the molar density mol/m^3. In this study ω (the number of moles of total precipitated species per kilogram of rock) is considered to be equal to 10 mol/kg (Pandey et al., 2014; Pandey and Chaudhuri, 2017)), and ρ_s equal to 2500 kg/m^3 (Jaeger et al., 2009). Note that this term, (24), enters (12). Also, the terms ϕ_m and ϕ_c are used to distinguish between the changes in ϕ due to solid deformation as in (23), and chemical reactions as in (24), respectively. The changes in porosity due to (23) and (24), also affect the specific surface area (A_s) as

$$A_s = A_0 \frac{\phi}{\phi_0}\frac{\log(\phi)}{\log(\phi_0)}, \tag{25}$$

where A_0 is the initial value of A_s, and it is set to 5000 throughout this study. This value is reported by Taheriotaghsara et al. (2020). Furthermore, the porosity change influences the matrix permeability

Table 1
Coefficients of the (21) for different range of (20).

	a_0	a_1	a_2	a_3	a_4	a_5
$\tilde{c} > 0.01$	−5.73	1.25×10^{-2}	1.38	2.61×10^{-5}	-4.01×10^{-3}	3.26×10^{-1}
$-0.01 < \tilde{c}$	−6.45	2.09×10^{-2}	-4.65×10^{-2}	3.06×10^{-5}	9.25×10^{-3}	-4.59×10^{-1}
$-0.01 < \tilde{c} \leq 0.01$	−5.80	1.35×10^{-2}	9.97×10^{-1}	3.80×10^{-5}	1.51×10^{-5}	-4.87×10^{-4}

Table 2
Summary of the effects of individual physical processes on physical properties.

Physical properties	Mechanical deformation	Fluid pressure	Calcite concentration
ϕ	(23)	(23)	(24)
$\boldsymbol{k}$	(23) + (26)	(23) + (26)	(24) + (26)
μ	–	–	(27)
$\boldsymbol{D}_e$	(23) + (15)	(23) + (15)	(24) + (15)
A_s	(23) + (25)	(23) + (25)	(24) + (25)

as (Rutqvist et al., 2002; Rutqvist and Stephansson, 2003; Min et al., 2004):

$$\boldsymbol{k} = \boldsymbol{k}_0 k_{mult}(\phi) = \boldsymbol{k}_0 \exp\left(b\left(\frac{\phi}{\phi_0} - 1\right)\right), \tag{26}$$

where $\boldsymbol{k}_0$ is the initial matrix permeability and b is an empirical parameter determined experimentally. In this work, we set $b = 22.2$ following the value reported by Rutqvist et al. (2002). The change in c also affects μ, and we adopt the specific form from Grolimund et al. (2001), Bijeljic and Blunt (2007) and Yortsos and Salin (2006), given by

$$\mu = \log(\mu_l) + \left(\frac{c - c_l}{c_h - c_l}\right)\left(\log(\mu_h) - \log(\mu_l)\right), \tag{27}$$

where c_l and c_h are lower and higher bounds of the concentration, and μ_l and μ_h are fluid viscosity corresponding to c_l and c_h, respectively. Table 2 summarizes the effects of physical processes on material properties considered in this study. Note that the numbers, e.g., (23), point out the equations used to represent these effects, while a hyphen means the absence of a relationship.

3. Numerical methods

In this section, we describe the numerical methods for the governing system described in the previous sections. Here, we utilize a combination of a mixed finite element method for spatial discretization, and employ both a backward differentiation formula and an explicit Runge–Kutta method for temporal discretization.

3.1. Domain discretization and geometrical quantities

We begin by introducing the notations used throughout this paper. Let $\mathcal{T}_h$ be a shape-regular triangulation obtained by a partition of Ω into d-simplices (triangles in $d = 2$, tetrahedra in $d = 3$). For each cell $T \in \mathcal{T}_h$, we denote by h_T the diameter of T, and we set $h = \max_{T\in\mathcal{T}_h} h_T$ and $h_l = \min_{T\in\mathcal{T}_h} h_T$. We further denote by $\mathcal{E}_h$ the set of all faces (i.e., $d-1$ dimensional entities connected to at least a $T \in \mathcal{T}_h$) and by $\mathcal{E}_h^I$ and $\mathcal{E}_h^\partial$ the collection of all interior and boundary facets, respectively. The boundary set $\mathcal{E}_h^\partial$ is decomposed as $\mathcal{E}_h^{D,u} \cup \mathcal{E}_h^{N,u}$, where $\mathcal{E}_h^{D,u}$ and $\mathcal{E}_h^{N,u}$ are two disjoint subsets associated with the Dirichlet boundary faces on $\partial\Omega_u$ and the Neumann boundary faces on $\partial\Omega_{tr}$ as defined in (7). Similarly, $\mathcal{E}_h^\partial$ is also decomposed as $\mathcal{E}_h^{D,m} \cup \mathcal{E}_h^{N,m}$, where $\mathcal{E}_h^{D,u}$ ($\mathcal{E}_h^{N,m}$, respectively) is associated to $\partial\Omega_p$ ($\partial\Omega_q$, resp.) in (12), as well as $\mathcal{E}_h^\partial = \mathcal{E}_h^{\text{In}} \cup \mathcal{E}_h^{\text{Out}}$, where $\mathcal{E}_h^{\text{In}}$ ($\mathcal{E}_h^{\text{Out}}$, resp.) is defined based on $\partial\Omega_{\text{In}}$ ($\partial\Omega_{\text{Out}}$, resp.) in (17).

We also define

$$e = \partial T^+ \cap \partial T^-, \quad e \in \mathcal{E}_h^I,$$

where T^+ and T^- are the two neighboring elements to e. We denote by h_e the characteristic length of e calculated as

$$h_e := \frac{\text{meas}(T^+) + \text{meas}(T^-)}{2\,\text{meas}(e)}, \tag{28}$$

depending on the argument, meas$(\cdot)$ represents the measure of a cell or of a facet.

Let $\mathbf{n}^+$ and $\mathbf{n}^-$ be the outward unit normal vectors to ∂T^+ and ∂T^-, respectively. For any given scalar function $\zeta : \mathcal{T}_h \to \mathbb{R}$ and vector function $\boldsymbol{\tau} : \mathcal{T}_h \to \mathbb{R}^d$, we denote by $\zeta^\pm$ and $\boldsymbol{\tau}^\pm$ the restrictions of ζ and $\boldsymbol{\tau}$ to $T^\pm$, respectively. Subsequently, we define the weighted average operator as

$$\{\zeta\}_{\delta e} = \delta_e \zeta^+ + (1 - \delta_e)\,\zeta^-, \quad \text{on } e \in \mathcal{E}_h^I, \tag{29}$$

and

$$\{\boldsymbol{\tau}\}_{\delta e} = \delta_e \boldsymbol{\tau}^+ + (1 - \delta_e)\,\boldsymbol{\tau}^-, \quad \text{on } e \in \mathcal{E}_h^I, \tag{30}$$

where δ_e is calculated by Ern et al. (2009) and Ern and Stephansen (2008):

$$\delta_e := \frac{k_e^-}{k_e^+ + k_e^-}. \tag{31}$$

Here,

$$k_e^+ := (\mathbf{n}^+)^\intercal \cdot \boldsymbol{k}^+ \mathbf{n}^+, \quad \text{and } k_e^- := (\mathbf{n}^-)^\intercal \cdot \boldsymbol{k}^- \mathbf{n}^-, \tag{32}$$

where k_e is a harmonic average of k_e^+ and k_e^- which reads

$$k_e := \frac{2k_e^+ k_e^-}{k_e^+ + k_e^-}, \tag{33}$$

and $\boldsymbol{k}$ is defined as in (11). The jump across an interior edge will be defined as

$$[\![\zeta]\!] = \zeta^+\mathbf{n}^+ + \zeta^-\mathbf{n}^- \quad \text{and} \quad [\![\boldsymbol{\tau}]\!] = \boldsymbol{\tau}^+ \cdot \mathbf{n}^+ + \boldsymbol{\tau}^- \cdot \mathbf{n}^- \quad \text{on } e \in \mathcal{E}_h^I.$$

Finally, for $e \in \mathcal{E}_h^\partial$, we set $\{\zeta\}_{\delta_e} := \zeta$ and $\{\boldsymbol{\tau}\}_{\delta_e} := \boldsymbol{\tau}$ for what concerns the definition of the weighted average operator, and $[\![\zeta]\!] := \zeta\mathbf{n}$ and $[\![\boldsymbol{\tau}]\!] := \boldsymbol{\tau} \cdot \mathbf{n}$ as definition of the jump operator.

3.2. Temporal discretization

The time domain $\mathbb{T} = (0, \mathrm{T}]$ is partitioned into N subintervals such that $0 =: t^0 < t^1 < \cdots < t^N := \mathrm{T}$. The length of each subinterval Δt^{n-1} is defined as $\Delta t^{n-1} = t^n - t^{n-1}$ where n represents the current time step. We assume that the user provides the initial Δt^0, while an adaptive procedure is carried out to choose Δt^{n-1}, $n > 1$, as follows:

$$\Delta t^{n-1} := \begin{cases} \text{CFL}\dfrac{h_l}{\|\boldsymbol{q}^{n-1}\|_\infty} & \text{if } \Delta t^n \leq \Delta t_{\max} \\ \Delta t_{\max} & \text{if } \Delta t^n > \Delta t_{\max}, \end{cases} \tag{34}$$

where CFL is a constant that the user can provide according to the Courant–Friedrichs–Lewy condition (Courant et al., 1967), $\|\cdot\|_\infty$ is the maximum norm of a vector function, and $\Delta t_{\max}$ is a maximum allowed time step. Note that we use $\Delta t_{\max}$ as a tool to control Δt^n as the model approaches a steady-state condition since $\|\boldsymbol{q}^{n-1}\|_\infty$ may approach zero, which would lead to a very large ratio $\frac{h_l}{\|\boldsymbol{q}^{n-1}\|_\infty}$.

Let $\varphi(\cdot,t)$ be a scalar function and φ^n be its approximation at time t^n, i.e. $\varphi^n \approx \varphi(t^n)$. We employ the following backward differentiation formula (Ibrahim et al., 2007; Akinfenwa et al., 2013; Lee et al., 2018)

$$\mathrm{BDF}_m(\varphi^n) := \begin{cases} \frac{1}{\Delta t^n}\left(\varphi^n - \varphi^{n-1}\right) & m=1 \\ \frac{1}{2\Delta t^n}\left(3\varphi^n - 4\varphi^{n-1} + \varphi^{n-2}\right) & m=2 \\ \frac{1}{6\Delta t^n}\left(11\varphi^n - 18\varphi^{n-1} + 9\varphi^{n-2} - 2\varphi^{n-3}\right) & m=3 \\ \frac{1}{12\Delta t^n}\left(25\varphi^n - 48\varphi^{n-1} + 36\varphi^{n-2} - 16\varphi^{n-3} + 3\varphi^{n-4}\right) & m=4 \end{cases} \tag{35}$$

for the discretization of the time derivative of $\varphi(\cdot,t)$ at time t^n. We also utilize the explicit Runge–Kutta methods (Dormand and Prince, 1980; Chen et al., 2006):

$$\mathrm{RK}_1(\varphi^n) = \varphi^{n+1} = \varphi^n + \kappa_1, \tag{36}$$

$$\kappa_1 = \Delta t^n F\left(\mathbb{X}^n, \mathbb{Y}^n\right),$$

for the first order Runge–Kutta method corresponding to the explicit Euler method, and

$$\mathrm{RK}_4(\varphi^n) = \varphi^{n+1} = \varphi^n + \frac{1}{6}\kappa_1 + \frac{1}{3}\kappa_2 + \frac{1}{3}\kappa_3 + \frac{1}{6}\kappa_4, \tag{37}$$

$$\begin{aligned} \kappa_1 &= \Delta t^n F\left(\mathbb{X}^n, \mathbb{Y}^n\right), \\ \kappa_2 &= \Delta t^n F\left(\mathbb{X}^n + \tfrac{1}{2}\Delta t^n, \mathbb{Y}^n + \tfrac{1}{2}\kappa_1\right), \\ \kappa_3 &= \Delta t^n F\left(\mathbb{X}^n + \tfrac{1}{2}\Delta t^n, \mathbb{Y}^n + \tfrac{1}{2}\kappa_2\right), \\ \kappa_4 &= \Delta t^n F\left(\mathbb{X}^n + \Delta t^n, \mathbb{Y}^n + \kappa_3\right), \end{aligned}$$

for the fourth order Runge–Kutta method, $F(\mathbb{X}^n, \mathbb{Y}^n)$ is any functions with independent variable $\mathbb{X}$ and dependent variable $\mathbb{Y}$ (Dormand and Prince, 1980; Chen, 2007), which we will specify in the linearization and solving processes in Section 3.4.

Finally, we define an extrapolation operator as follows (Chen et al., 2006; Chen, 2007):

$$\mathrm{EX}(\varphi) = \hat{\varphi}^{n+1} = \begin{cases} \left(1 + \frac{\Delta t^n}{\Delta t^{n-1}}\right)\varphi^n - \frac{\Delta t^n}{\Delta t^{n-1}}\varphi^{n-1} & \text{if } n \geq 1, \\ \varphi^0 & \text{if } n = 0, \end{cases} \tag{38}$$

and in the following we will adopt the notation $\hat{\varphi}^{n+1}$ to denote an extrapolation value of $\{\varphi^n, \varphi^{n-1}\}$.

3.3. Spatial discretization

In this framework, the displacement field is approximated by the classical continuous Galerkin method (CG) method, and the fluid velocity and pressure fields are discretized by the Brezzi–Douglas–Marini (BDM) element (Brezzi and Fortin, 2012) and the piecewise constants discontinuous Galerkin (DG) method, respectively, to ensure local mass conservation. Lastly, the concentration field is discretized by the enriched Galerkin (EG) method (Lee et al., 2016; Sun and Liu, 2009).

To begin, we define the finite element space for the CG function space for a vector-valued function:

$$\mathcal{U}_h^{\mathrm{CG}_k}(\mathcal{T}_h) := \left\{\boldsymbol{\psi_u} \in \mathbb{C}^0(\Omega;\mathbb{R}^d) : \boldsymbol{\psi_u}\big|_T \in \mathbb{P}_k(T;\mathbb{R}^d), \forall T \in \mathcal{T}_h\right\}, \tag{39}$$

where $\mathbb{C}^0(\Omega;\mathbb{R}^d)$ denotes the space of vector-valued piecewise continuous polynomials, $\mathbb{P}_k(T;\mathbb{R}^d)$ is the space of polynomials of degree at most k over each element T, and $\boldsymbol{\psi_u}$ denotes a generic function of $\mathcal{U}_h^{\mathrm{CG}_k}(\mathcal{T}_h)$. In addition, the CG space for scalar-valued functions is defined as:

$$\mathcal{P}_h^{\mathrm{CG}_k}(\mathcal{T}_h) := \left\{\psi_p \in \mathbb{C}^0(\Omega) : \psi_p\big|_T \in \mathbb{P}_k(T), \forall T \in \mathcal{T}_h\right\}, \tag{40}$$

where $\mathbb{C}^0(\Omega) := \mathbb{C}^0(\Omega;\mathbb{R})$ and $\mathbb{P}_k(T) := \mathbb{P}_k(T;\mathbb{R})$. Next, we define the following DG function space:

$$\mathcal{P}_h^{\mathrm{DG}_k}(\mathcal{T}_h) := \left\{\psi_p \in L^2(\Omega) : \psi_p\big|_T \in \mathbb{P}_k(T), \forall T \in \mathcal{T}_h\right\}, \tag{41}$$

where $L^2(\Omega)$ is the space of square-integrable scalar functions. We then define the EG finite element space with polynomial order k as:

$$\mathcal{P}_h^{\mathrm{EG}_k}(\mathcal{T}_h) := \mathcal{P}_h^{\mathrm{CG}_k}(\mathcal{T}_h) \oplus \mathcal{P}_h^{\mathrm{DG}_0}(\mathcal{T}_h), \tag{42}$$

i.e., a CG finite element space enriched by the space $\mathcal{P}_h^{\mathrm{DG}_0}(\mathcal{T}_h)$ of piecewise constant functions. In the following we denote ψ_c a generic function of $\mathcal{P}_h^{\mathrm{EG}_k}(\mathcal{T}_h)$.

Lastly, we define the BDM function space as follows (Brezzi and Fortin, 2012):

$$\mathcal{V}_h^{\mathrm{BDM}_k}(\mathcal{T}_h) := \left\{\boldsymbol{\psi_v} \in H(\mathrm{div},\Omega) : \boldsymbol{\psi_v}\big|_T \in \mathrm{BDM}(T), \forall T \in \mathcal{T}_h\right\} \tag{43}$$

where $\boldsymbol{\psi_v}$ denotes a generic function of $\mathcal{V}_h^{\mathrm{BDM}_k}(\mathcal{T}_h)$ and $\mathrm{BDM}(T)$ is defined according to Brezzi and Fortin (2012):

$$\begin{aligned} &T \in \{\text{ triangle, tetrahedron }\} \\ &\mathcal{V} = \left[\mathcal{P}_q(T)\right]^d \\ &\mathcal{L} = \begin{cases} \int_f v\cdot\mathbf{n}p\,dS, & \text{for a set of basis functions } p \in \mathcal{P}_q(f) \\ & \text{for each facet} \\ \int_T v\cdot p\,dx, & \text{for set of basis functions } p \in \mathrm{NED}_{k-1}(T) \\ & \text{for } k \geqslant 2 \end{cases} \end{aligned} \tag{44}$$

where NED refers to the Nédélec elements of the first kind.

3.3.1. Fully discrete form

We now present the fully discrete form of the coupled HMC problem using the above-described combination of finite element spaces. In particular, we seek the approximated displacement solution $\boldsymbol{u_h} \in \mathcal{U}_h^{\mathrm{CG}_2}(\mathcal{T}_h)$ as done in Choo and Lee (2018), Kadeethum et al. (2019a) and Vik et al. (2018), fluid pressure $p_h \in \mathcal{P}_h^{\mathrm{DG}_0}(\mathcal{T}_h)$, velocity approximation $\boldsymbol{q}_h \in \mathcal{V}_h^{\mathrm{BDM}_1}(\mathcal{T}_h)$, and concentration approximation $c_h \in \mathcal{P}_h^{\mathrm{EG}_1}(\mathcal{T}_h)$.

We multiply the linear momentum balance equation (7) by a test function $\boldsymbol{\psi_u} \in \mathcal{U}_h^{\mathrm{CG}_2}(\mathcal{T}_h)$. The fully discretized linear momentum balance equation thus has the following form:

$$\mathcal{N}_u\left(\boldsymbol{\psi_u}; \boldsymbol{u}_h^n, p_h^n\right) = 0, \quad \forall \boldsymbol{\psi_u} \in \mathcal{U}_h^{\mathrm{CG}_2}(\mathcal{T}_h), \tag{45}$$

at each time step t^n, where

$$\begin{aligned} &\mathcal{N}_u\left(\boldsymbol{\psi_u}; \boldsymbol{u}_h^n, p_h^n\right) \\ &= \sum_{T\in\mathcal{T}_h}\int_T \boldsymbol{\sigma}'\left(\boldsymbol{u}_h^n\right) : \nabla^s\boldsymbol{\psi_u}\,dV - \sum_{T\in\mathcal{T}_h}\int_T \alpha p_h^n\mathbf{I} : \nabla^s\boldsymbol{\psi_u}\,dV \\ &\quad - \sum_{T\in\mathcal{T}_h}\int_T \boldsymbol{f}\boldsymbol{\psi_u}\,dV - \sum_{e\in\mathcal{E}_h^{N,u}}\int_e \boldsymbol{t_D}\boldsymbol{\psi_u}\,dS, \quad \forall\boldsymbol{\psi_u} \in \mathcal{U}_h^{\mathrm{CG}_2}(\mathcal{T}_h) \end{aligned}$$

Here $\int_T \cdot\, dV$ and $\int_e \cdot\, dS$ refer to volume and surface integrals, respectively, and ∇^s is the symmetric gradient operator. Furthermore, the notation for $\mathcal{N}_u\left(\boldsymbol{\psi_u}; \boldsymbol{u}_h^n, p_h^n\right)$ in (45) highlights before the semicolon the test function, and after the semicolon the (possibly nonlinear) dependence on discrete solutions to the coupled problem. The same notation will be used hereafter for the remaining equations.

Next, the weak form of the mass balance equation (12) is obtained multiplying by $\psi_p \in \mathcal{P}_h^{\mathrm{DG}_0}(\mathcal{T}_h)$ and integrating by parts, resulting in:

$$\mathcal{N}_p\left(\psi_p; p_h^n, \boldsymbol{q}_h^n, c_h^n\right) = 0, \quad \forall\psi_p \in \mathcal{P}_h^{\mathrm{DG}_0}(\mathcal{T}_h), \tag{46}$$

for each time step t^n, where

$$\begin{aligned} &\mathcal{N}_p\left(\psi_p; p_h^n, \boldsymbol{q}_h^n, c_h^n\right) \\ &= \sum_{T\in\mathcal{T}_h}\int_T \left(\frac{1}{M} + \frac{\alpha^2}{K}\right)\mathrm{BDF}_1\left(p_h^n\right)\psi_p\,dV + \sum_{T\in\mathcal{T}_h}\int_T \nabla\cdot\left(\boldsymbol{q}_h^n\right)\psi_p\,dV \\ &\quad + \sum_{T\in\mathcal{T}_h}\int_T \frac{\alpha}{K}\mathrm{RK}_1(\sigma_v)\psi_p\,dV + \sum_{T\in\mathcal{T}_h}\int_T \mathrm{RK}_1(\phi_c)\psi_p\,dV \\ &\quad - \sum_{T\in\mathcal{T}_h}\int_T g\psi_p\,dV. \end{aligned}$$

For the Darcy velocity equation (10), we obtain

$$\mathcal{N}_v\left(\boldsymbol{\psi}_v; \boldsymbol{u}_h^n, p_h^n, \boldsymbol{q}_h^n, c_h^n\right) = 0, \quad \forall \boldsymbol{\psi}_v \in \mathcal{V}_h^{\mathrm{BDM}_1}\left(\mathcal{T}_h\right). \tag{47}$$

where

$$\begin{aligned}\mathcal{N}_v\left(\boldsymbol{\psi}_v; \boldsymbol{u}_h^n, p_h^n, \boldsymbol{q}_h^n, c_h^n\right) :=& \sum_{T\in\mathcal{T}_h}\int_T p_h^n \nabla\cdot\boldsymbol{\psi}_v \, dV \\ &+ \sum_{T\in\mathcal{T}_h}\int_T \boldsymbol{k}(\boldsymbol{u}_h^n, c_h^n)^{-1}\mu(c_h^n)\boldsymbol{q}_h^n\boldsymbol{\psi}_v \, dV \\ &+ \sum_{e\in\mathcal{E}_h^{D,m}}\int_e p_D\boldsymbol{\psi}_v\cdot\mathbf{n}\, dS.\end{aligned}$$

Lastly, for the advection–diffusion–reaction equations of species transport we write:

$$\mathcal{N}_c\left(\psi_c; \boldsymbol{u}_h^n, \boldsymbol{q}_h^n, c_h^n\right) = 0, \quad \forall\psi_c \in \mathcal{P}_h^{\mathrm{EG}_1}\left(\mathcal{T}_h\right) \tag{48}$$

for each time step t^n, where

$$\begin{aligned}&\mathcal{N}_c\left(\psi_c; \boldsymbol{u}_h^n, \boldsymbol{q}_h^n, c_h^n\right) \\ &= \sum_{T\in\mathcal{T}_h}\int_T \phi\mathrm{BDF}_4\left(c_h^n\right)\psi_c \, dV + \sum_{T\in\mathcal{T}_h}\int_T \boldsymbol{D}_e{}^*(\phi^n)\nabla c_h^n\cdot\nabla\psi_c \, dV \\ &\quad - \sum_{e\in\mathcal{E}_h^I}\int_e \left\{\boldsymbol{D}_e{}^*(\phi^n)\nabla c_h^n\right\}_{\delta_e}\cdot[\![\psi_c]\!]\, dS \\ &\quad + \theta\sum_{e\in\mathcal{E}_h^I}\int_e \left\{\boldsymbol{D}_e{}^*(\phi^n)\nabla\psi_c\right\}_{\delta_e}\cdot[\![c_h^n]\!]\, dS \\ &\quad + \sum_{e\in\mathcal{E}_h^I}\int_e \frac{\beta}{h_e}\boldsymbol{D}_e{}^*(\phi^n)_e[\![c_h^n]\!]\cdot[\![\psi_c]\!]\, dS \\ &\quad - \sum_{T\in\mathcal{T}_h}\int_T \boldsymbol{q}_h^n c_h^n\cdot\nabla\psi_c \, dV + \sum_{e\in\mathcal{E}_h^I}\int_e \boldsymbol{q}_h^n\cdot\mathbf{n}c_h^{\mathrm{up}}[\![\psi_c]\!]\, dS \\ &\quad + \sum_{e\in\mathcal{E}_h^{\mathrm{Out}}}\int_e \boldsymbol{q}_h^n\cdot\mathbf{n}c_h^n\psi_c \, dS \\ &\quad - \sum_{T\in\mathcal{T}_h}\int_T R_c A_s\psi_c \, dV + \sum_{e\in\mathcal{E}_h^{\mathrm{In}}}\int_e \boldsymbol{q}_h^n\cdot\mathbf{n}c_{\mathrm{in}}\psi_c \, dS.\end{aligned}$$

We note that the $\boldsymbol{D}_e{}^*(\phi^n)$ is redefining $\boldsymbol{D}_e(\phi^n)$ by including the numerical stabilization term, where

$$\boldsymbol{D}_e{}^*(\phi^n) := \boldsymbol{D}_e(\phi^n) + \gamma h\left\|\boldsymbol{q}_h^n\right\|\mathbf{I}, \tag{49}$$

as defined in Araya et al. (2005), Harari and Hughes (1994) and Masud and Khurram (2004). The $\gamma h\left\|\boldsymbol{q}_h^n\right\|\mathbf{I}$ term is often referred as the first order artificial diffusivity coefficient (Onate, 1998; Brezzi et al., 1992). In our paper, we set the tuning parameter $\gamma = 0.25$. Alternative stabilization strategies including streamline diffusion and crosswind diffusion, or entropy viscosity methods could be also utilized to reduce oscillations in the numerical solution to the concentration field (Bonito et al., 2014; Araya et al., 2005; Harari and Hughes, 1994; Masud and Khurram, 2004; Brezzi et al., 1992; Guermond et al., 2019; Scovazzi et al., 2017; Lee and Wheeler, 2017).

Also, c_h^{up} is an upwind value of c_h^n defined as (Riviere and Wheeler, 2000; Riviere, 2008):

$$c_h^{\mathrm{up}} = \begin{cases} c_h^{n+} & \text{if} \quad \boldsymbol{q}_h^n\cdot\mathbf{n} \geq 0 \\ c_h^{n-} & \text{if} \quad \boldsymbol{q}_h^n\cdot\mathbf{n} < 0 \end{cases} \quad \forall e = \partial T^+\cap\partial T^- \tag{50}$$

where c_h^{n+} and c_h^{n-} correspond to c_h^n of T^+ and T^-, respectively.

Lastly, the two parameters θ and β define corresponding interior penalty methods. The discretization becomes the symmetric interior penalty Galerkin method (SIPG) when $\theta = -1$, the incomplete interior penalty Galerkin method (IIPG) when $\theta = 0$, and the non-symmetric interior penalty Galerkin method (NIPG) when $\theta = 1$ (Riviere, 2008). In this study, we set $\theta = -1$ for the simplicity and $\beta = 1.1$ throughout this paper.

Remark 1. For the momentum balance equation (7), the traction boundary condition $\boldsymbol{t}_D$ (traction) is applied weakly on each $e \in \mathcal{E}_h^{N,u}$ in (45), while the displacement boundary condition $\boldsymbol{u}_D$ is strongly enforced on each $e \in \mathcal{E}_h^{D,u}$. For the mass balance equation (12), since we use a mixed formulation, the flux boundary condition q_D is strongly applied on each $e \in \mathcal{E}_h^{N,m}$, but the pressure boundary condition p_D is weakly applied on each $\mathcal{E}_h^{D,m}$ in (47). Finally, for the transport equation (17), all boundary conditions are weakly applied in (48).

Remark 2. In our computational framework, we provide a flexible choice of the time discretization schemes for each equation. We use BDF_1 for the time discretization of the mass balance equation (12) since it is sufficient to provide the optimal error convergence rate, see Zhang et al. (2016). For the time discretization of the transport equation (17), we use BDF_4 to capture a sharp front in the advection dominated regime (Riviere, 2008).

3.4. Splitting algorithm

The coupled system obtained from the discrete governing equations (45), (46), (47), and (48) is nonlinear. Although the coupled nonlinear system may be solved in a monolithic manner, here we focus on developing a splitting algorithm for sequential solution to the coupled system, which can provide more flexibility especially when different software packages need to be combined. The overall computational strategy is summarized in Algorithm 1.

Algorithm 1 Splitting algorithm for hydro-mechanical–chemical coupling model

1: Initialize all input parameters ▷ p_0 and c_0 must be provided.
2: Solve the equilibrium state for $\boldsymbol{u_0}$ ▷ see (45)
3: Update ϕ^0, $\boldsymbol{k}^0$, $\boldsymbol{D}_e^0$, and A_s^0 ▷ see (23), (26), (15), (25)
4: **for each** time step t^n **do**
5: *Part 1: coupling solid and fluid mechanics*
6: Set $\iota \to 0$ as the nonlinear iterations counter
7: $p_h^{n-1} \to p_h^{n,\iota=0}$, $\boldsymbol{q}_h^{n-1} \to \boldsymbol{q}_h^{n,\iota=0}$, $\boldsymbol{u}_h^{n-1} \to \boldsymbol{u}_h^{n,\iota=0}$
8: **for each** fixed stress iteration step $(\cdot)^{n,\iota}$ until $\delta\phi^{n,\iota} <$ TOL **do**
9: Solve (46) and (47) w.r.t. p_h^n and $\boldsymbol{q}_h^n$ for fixed $\boldsymbol{u}_h^n := \boldsymbol{u}_h^{n,\iota-1}, c_h^n := \hat{c}_h^n$ to get $p_h^{n,\iota}, \boldsymbol{q}_h^{n,\iota}$
10: Calculate $\phi_f^{n,\iota}$ ▷ see (52)
11: Solve (45) w.r.t. $\boldsymbol{u}_h^n$ and for fixed $p_h^n := p_h^{n,\iota}$ to get $\boldsymbol{u}_h^{n,\iota}$
12: Calculate $\phi_m^{n,\iota}$ ▷ see (23)
13: Evaluate $\mathrm{F}\left(\dot{\sigma_v}^{n,\iota}\right)$ ▷ see (53)
14: Evaluate $\delta\phi^{n,\iota}$ ▷ see (51)
15: Update $\boldsymbol{k}^{n,\iota}$ ▷ see (23), (26)
16: **end for**
17: $p_h^{n,\iota} \to p_h^n$, $\boldsymbol{q}_h^{n,\iota} \to \boldsymbol{q}_h^n$, $\boldsymbol{u}_h^{n,\iota} \to \boldsymbol{u}_h^n$
18: *Part 2: chemical process*
19: Update ϕ^n, $\boldsymbol{D}_e^n$, and A_s^n ▷ see (23), (15), (25)
20: Solve (48) w.r.t. c_h^n for fixed $\boldsymbol{u}_h^n := \boldsymbol{u}_h^n, \boldsymbol{q}_h^n := \boldsymbol{q}_h^n$ to get c_h^n
21: Extrapolate $\hat{c}_h^{n+1}$ ▷ see (54)
22: Calculate Δt^{n+1} ▷ see (34)
23: Evaluate $\mathrm{F}\left(\hat{q}^{n+1}\right)$ and $\mathrm{F}\left(\hat{\phi}_c^{n+1}\right)$ ▷ see (56), (55)
24: Update $\hat{\phi}^{n+1}$, $\hat{\boldsymbol{k}}^{n+1}$, $\hat{\boldsymbol{D}}_t^{n+1}$, $\hat{\mu}^{n+1}$, and $\hat{A}_s{}^{n+1}$ ▷ see (54), (24), (26), (15), (27), (25)
25: $p_h^n \to p_h^{n-1}$, $\boldsymbol{q}_h^n \to \boldsymbol{q}_h^{n-1}$, $\boldsymbol{u}_h^n \to \boldsymbol{u}_h^{n-1}$, $c_h^n \to c_h^{n-1}$ ▷ update time step $n-1$
26: Output
27: **end for**

In Algorithm 1, we separate our algorithm into two parts. The first part (lines 8 to 17) focuses on solving the coupled hydro-mechanical problem, (45), (46), and (47), using the fixed stress method which is an unconditionally stable splitting scheme (Kim et al., 2011; Dana and

Wheeler, 2018; Dana et al., 2018; Mikelic and Wheeler, 2013). At each iteration ι we solve (46) and (47) for the velocity $\boldsymbol{q}_h^{n,\iota}$ and the pressure $p_h^{n,\iota}$ using a monolithic method (line 9) based on given displacement $\boldsymbol{u}_h^{n,\iota-1}$ from previous nonlinear iteration and concentration extrapolated $\hat{c}_h^n$ from previous time step. Then, we couple with (45) using the fixed-stress split scheme based on the pressure $p_h^{n,\iota}$ computed at the current nonlinear iteration (line 11). The convergence criterion is based on $\delta\phi^{n,\iota}$ (Algorithm 1 line 8), which is defined as:

$$\delta\phi^{n,\iota} := \frac{\phi_m^{n,\iota} - \phi_f^{n,\iota}}{\phi_m^{n,\iota}}. \tag{51}$$

Here, $\phi_m^{n,\iota}$ is the porosity resulting from the solid deformation (23) and $\phi_f^{n,\iota}$ is the porosity resulting from the fluid flow problem defined as (Mikelic and Wheeler, 2013; Dana and Wheeler, 2018; Dana et al., 2018):

$$\phi_f^{n,\iota} = \phi^{n-1} + \frac{(\alpha - \phi^{n-1})}{K}\left(p^{n,\iota} - p^{n-1}\right), \tag{52}$$

where $(\cdot)^\iota$ represents iteration counter inside the fixed-stress loop. From the fixed stress split concept (52) is the ϕ predictor, while (23) is the ϕ corrector (Kim et al., 2011; Dana and Wheeler, 2018; Dana et al., 2018; Mikelic and Wheeler, 2013). Hence, when $\phi_m^{n,\iota}$ and $\phi_f^{n,\iota}$ converge, i.e., $\delta\phi^{n,\iota} < \mathrm{TOL}$, the fixed-stress loop is completed. The tolerance TOL is set as 1×10^{-6} throughout this study. Note that the flow equations, (46) and (47), are solved by assuming that $\frac{\partial \sigma_v}{\partial t} = 0$, i.e., $\mathrm{F}\left(\dot{\sigma_v}^{n,\iota}\right)$ is frozen; therefore, this term is evaluated explicitly after the momentum equation (45) is solved, as illustrated in Algorithm 1 line 13 (Kim et al., 2011; Mikelic and Wheeler, 2013), and $\mathrm{F}\left(\dot{\sigma_v}^{n,\iota}\right)$ is defined as:

$$\mathrm{F}\left(\dot{\sigma_v}^{n,\iota}\right) := \sum_{T\in\mathcal{T}_h}\int_T \frac{\alpha}{K}\mathrm{RK}_1\left(\sigma_v(\boldsymbol{u}^{n,\iota}, \boldsymbol{u}^{n-1}, p^{n,\iota}, p^{n-1})\right)\psi_p\, dV. \tag{53}$$

The second part (from line 18) focuses on solving advection-diffusion–reaction equation (48), using $\boldsymbol{q}_h^n$, ϕ^n, $\boldsymbol{D}_e^n$, and A_s^n obtained from the first part. One could view this strategy as a one-way coupling scheme between coupled hydro-mechanical and advection–diffusion–reaction equations. Next, Algorithm 1 line 21 linearizes c_h^{n+1} by extrapolating c_h^n and c_h^{n-1} to $\hat{c}_h^{n+1}$ by using (38):

$$\hat{c}_h^{n+1} = \mathrm{EX}\left(c_h\right) \tag{54}$$

where $\hat{(\cdot)}^n$ represents an extrapolation value based on the extrapolation described in (38). Subsequently, we evaluate $\mathrm{F}\left(\dot{\phi_c}^{n,\iota}\right)$ and $\mathrm{F}(q^{n,\iota})$, which are defined as

$$\mathrm{F}\left(\hat{\dot{\phi}}_c^{n+1}\right) := \sum_{T\in\mathcal{T}_h}\int_T \mathrm{RK}_1\left(\phi_c(\hat{c}^{n+1}, c^n)\right)\psi_p\, dV, \tag{55}$$

and

$$\mathrm{F}\left(\hat{q}^{n+1}\right) := \sum_{T\in\mathcal{T}_h}\int_T R_c(\hat{c}^{n+1}, p^n)A_s(\hat{c}^{n+1}, \boldsymbol{u}^n)\psi_c\, dV, \tag{56}$$

using $\hat{c}_h^{n+1}$ calculated by (54). We note that Eq. (48) becomes linear by employing $\hat{c}_h^{n+1}$ to calculate $\mathrm{F}(q)$. Also, the porosity alteration as a result of calcite dissolution/precipitation (Algorithm 1 line 24) is computed by

$$\hat{\phi}^{n+1} = \hat{\phi}_c^{n+1} = \mathrm{RK}_4\left(\Gamma\left(\boldsymbol{u}^n, \hat{c}_h^{n+1}\right)\right). \tag{57}$$

Note that the porosity change due to the calcite dissolution/precipitation reactions is additional to the porosity change by solid deformation, (23). Subsequently, $\hat{\boldsymbol{k}}^{n+1}$, $\hat{\boldsymbol{D}}_t^{n+1}$, and $\hat{A_s}^{n+1}$ are determined using $\hat{\phi}^{n+1}$. Lastly, we also calculate $\hat{\mu}^{n+1}$ using $\hat{c}_h^{n+1}$, see (54) and (27).

For all the computations, matrices and vectors are built using the FEniCS form compiler (Alnaes et al., 2015). The block structure is assembled by using the multiphenics toolbox (Ballarin and Rozza, 2019). Solvers are employed from PETSc package (Balay et al., 2018). All simulations are computed on XeonE5_2650v4 with a single thread.

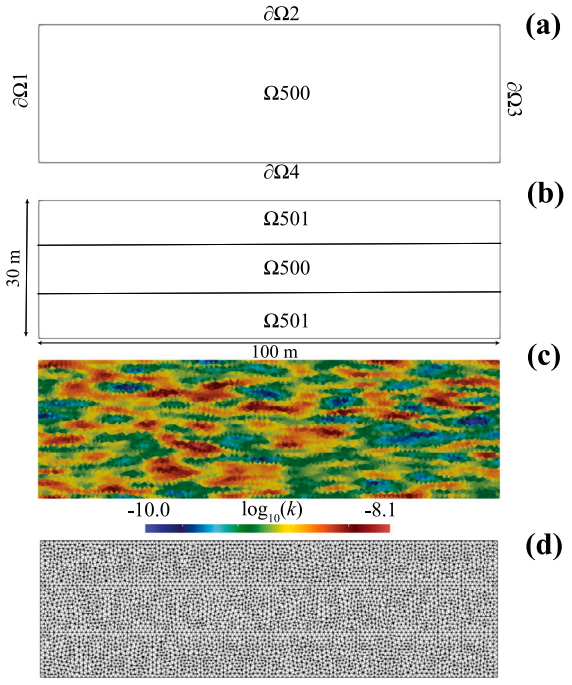

Fig. 1. Geometry and notation used to define material properties; (**a**) example 1: single-layer porous medium (Ω_{500}), (**b**) example 2: three-layer porous medium (Ω_{500} and Ω_{501}), (**c**) example 3: heterogeneous porous medium (the arithmetic mean of $\boldsymbol{k} = 8.8{\times}10^{-10}\mathbf{I}$ m^2 with correlation length in x- and y-direction of 5 and 1 m, respectively). (**d**) mesh 1 is used for all examples (number of element is 7852, and $h = 1.47$ m) unless otherwise stated.

Remark 3. We note that the EG method, which is used to approximate the advection–diffusion–reaction (17), is based on the Galerkin method, which could be extended to consider adaptive meshes that contain hanging nodes. Besides, an adaptive enrichment, i.e., the piecewise-constant functions only added to the elements where the sharp material discontinuities are observed, can be developed.

4. Numerical examples

In this section, we demonstrate the performance and capabilities of the proposed numerical method through various numerical examples. We begin with a single-layer model comparing the performance for single-phase flow with chemical dissolution/precipitation and solid deformation. Then we illustrate the performance of the developed model for a layered medium as well as a heterogeneous single-layer medium. Lastly, we test the proposed framework using an example with an anisotropic permeability field. All four examples and their mesh are illustrated in Fig. 1. More detailed setup, including the input parameters and the boundary conditions of each example, are described in the beginning of each example.

4.1. Example 1

In the first example, the computational domain is defined as $\Omega_{500} = [0, 100] \times [0, 30]$, which presents a single layer as shown in Fig. 1a. Following the physical properties of carbonate rock reported in Jaeger et al. (2009) and Medetbekova et al. (2020), we set $K = 8.4$ GPa, $\alpha = 0.74$, $\nu = 0.18$, $\phi = 0.2$, $\boldsymbol{k} = 8.8 \times 10^{-10}\mathbf{I}$ m^2. The fluid properties are $c_f = 1.0 \times 10^{-10}$ Pa^{-1}, $\rho = 1000$ kg/m^3, $\boldsymbol{D} = 1.0 \times 10^{-12}$ m^2/s, and μ is calculated using (27) by setting $\mu_h = 5.0$ and $\mu_l = 1.0 \times 10^{-4}$ Pa/s corresponding to $c_h = 1.68$ and $c_l = 0.0$ mmol/m^3, respectively. Next, the boundary conditions for all these examples are applied as follows. For the momentum balance equation (7), we assume $\boldsymbol{u}_D \cdot \mathbf{n} = 0$ on

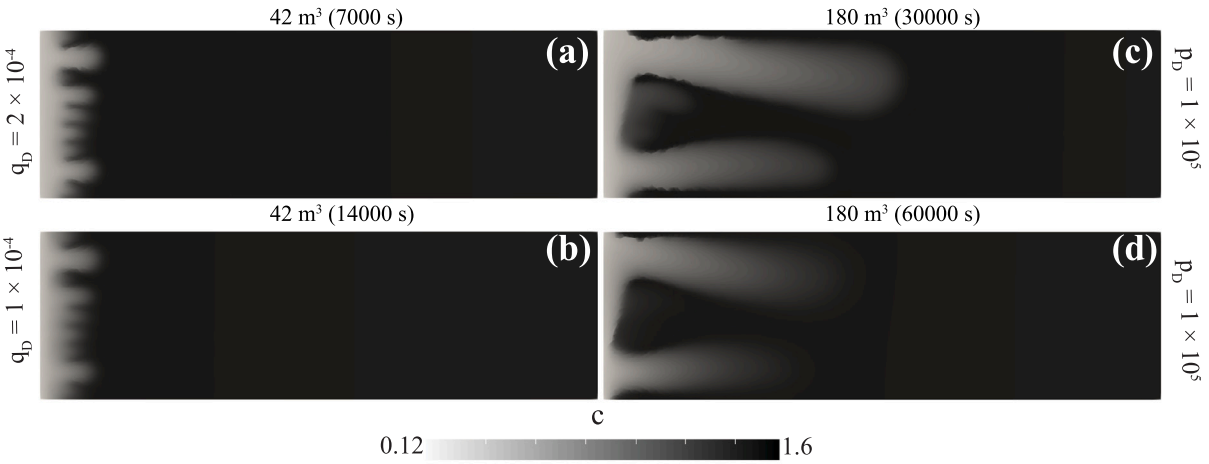

Fig. 2. Example 1: concentration fields, c; I.V. = 42 m^3 using **(a)** $q_D = 2\times10^{-4}$ m/s at $\partial\Omega_1$ and **(b)** $q_D = 1\times10^{-4}$ m/s at $\partial\Omega_1$; and I.V. = 180 m^3 using **(c)** $q_D = 2\times10^{-4}$ m/s at $\partial\Omega_1$ and **(d)** $q_D = 1\times10^{-4}$ m/s at $\partial\Omega_1$. The boundary conditions shown in this picture are corresponding to $\partial\Omega_1$ and $\partial\Omega_3$ of the mass balance equation (12).

$\partial\Omega_1$, $\partial\Omega_3$, and $\partial\Omega_4$. Furthermore, $\boldsymbol{t}_D = \left[0.0, -2.0\times10^6\right]$ Pa is applied on $\partial\Omega_2$. Therefore, the medium is under compression. For the mass balance equation (12), the boundary condition $q_D = 0$ is set on $\partial\Omega_2$ and $\partial\Omega_4$ and we impose $p_D = 1\times10^5$ Pa on $\partial\Omega_3$. Here, for the mass balance equation (12), we test two different scenarios on $\partial\Omega_1$, where scenario (a) corresponds to $q_D = 2\times10^{-4}$ m/s and scenario (b) is characterized by $q_D = 1\times10^{-4}$ m/s. Thus, scenarios (a) and (b) will be referred to as the high and low injection rate cases, respectively. Since we want to compare the results of the above scenarios at the same total injected volume (I.V.), which is defined as

$$\text{I.V.} = q_D t^n A_{\text{d}}, \tag{58}$$

where $A_{\text{d}} = 30\text{m}^2$ is the surface area of $\partial\Omega_1$, the time t^n of the scenario (b) is twice to scenario (a). For the advection–diffusion–reaction equation (17), we impose the inflow condition $c_{in} = 0.5$ on $\partial\Omega_1$. The initial pressure p_0 is 1×10^6 Pa, the initial concentration c_0 is calculated by (22) using $p = p_0$ and $\tau = 20$ C, and the initial displacement $\boldsymbol{u}_0$ is calculated as stated in Algorithm 1. The penalty parameter (β) is set to be 1.1 for the EG method. The CFL is used as 0.1 for calculating Δt^n, see (34).

Here, we compare the transient distribution of the concentration achieved with the developed HMC coupled numerical scheme in a homogeneous porous medium for two different injection rates. The aim is to illustrate the impact of different processes on the advance of the flow path and reactive solute transport. Initially, the composition of the pore fluid within the porous medium is in equilibrium with calcite. Note that c_{eq} calculated by (22) is a function of temperature and pressure. In this example, assuming constant temperature, pressure deviates from the initial fluid pressure in time and space. The changes in the pressure field as a result of fluid injection on the left boundary and the fluid production on the right boundary varies the c_{eq} resulting in precipitation or dissolution in the domain. The injected water is also unsaturated with respect to calcite. Therefore, the injected fluid, as advances into the domain, will dissolve the calcite mineral.

Fig. 2 shows the concentration fields at different injected fluid volumes (I.V.) and for both scenarios associated to q_D. There are three main observations from these figures. The first one is the flow instability, or fingering, emerged as a result of the difference between the injected fluid viscosity and the in-situ fluid viscosity. The second observation is that for the higher injection rate scenario, the fingers are more developed at a later time compared to that of the low injection scenario. The third one is that most of the fingers developed initially either merge or vanishes at the later stage, forming one or two main fingers.

Next, We use different mesh sizes to study the impact of mesh size on the observed fingering in Fig. 2. Two new meshes are used here: a coarse mesh and a fine mesh compared to mesh 1 illustrated in Fig. 1d. Note that the number of element is 3180 and $h = 2.01$ m for the coarse mesh, and the number of element is 14024 and $h = 1.10$ m for the fine mesh. The c fields of two different meshes are presented in Fig. 3. Comparing among Figs. 2a, 3a, and 3b, we observe that the early behavior are approximately similar. While the c field of the coarse mesh (compared to mesh 1 illustrated in Fig. 1d) is more uniformly developed with less number of initial fingers , the c field of the coarse mesh progresses to approximately similar distance as in the models with the finer meshes. The impact of mesh size on the fingering at a later time becomes less. This is evident by comparing Figs. 2c, 3c, and 3d.

Next, we present the interaction among different processes including mechanical deformation, calcite dissolution/precipitation, and viscosity alteration in Fig. 4 for two different time steps. Note that the results of the low injection rate case are similar (for the same volume of injected fluid); hence, we present here only the results of the high injection rate case. First, one could observe that the effect of mechanical deformation is dictated by both p and $\boldsymbol{u}$, see Fig. 4b and g. Fig. 4a and f illustrate the reduction of ϕ by the solid deformation as the model is under compression. The increased fluid pressure by fluid injection, however, limits the porosity reduction. This is reflected in Figs. 4a and f in which $\frac{\partial\phi_m}{\partial t}$ is positive in the left part of the domain and negative in the right part of the domain.

The $\frac{\partial\phi_c}{\partial t}$ result is shown in Fig. 4c and h. Since the injected concentration $c_{in} = 0.5$ is lower than c_0 (initial c_{eq}), the porous medium is dissolved in places to which the injected fluid is transported. Note that $\frac{\partial\phi_c}{\partial t}$ is positive where the dissolution occurs and negative where the perception occurs. At this time step, the maximum magnitude of $\frac{\partial\phi_c}{\partial t}$ is 10^{-7}, which is much less compared to that of $\frac{\partial\phi_m}{\partial t}$, which is around 10^{-4}. We note this magnitude could be varied with different input parameters and boundary conditions of each equation, (7), (12), or (17). The value of μ is also altered, see Fig. 4d and i, as the concentration front progresses. This alteration causes the flow instability discussed previously and establishes a preferential flow path. The impact of $\frac{\partial\phi_m}{\partial t}$, $\frac{\partial\phi_c}{\partial t}$, and μ alteration can be seen in $\boldsymbol{q}$ field shown in Fig. 4e and j. Interestingly, as the first finger reaches the outlet boundary the second finger gradually disappears resulting in only one preferential path between the inlet and outlet of the model.

Thus, we have confirmed that the proposed framework can well simulate the expected physical and chemical phenomena including solid deformation, viscous fingering, and dissolution/precipitation. The key ingredients of this method are the capability for tracking the interface of the concentration species approximated by the high order methods with numerical stabilization, the computation of reaction terms with the EG method, and the locally conservative flux from BDM.

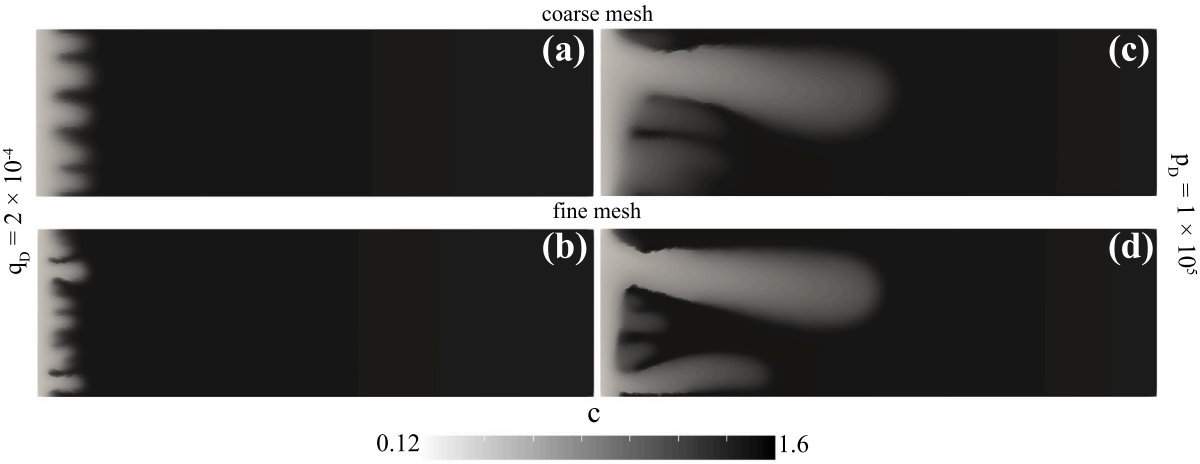

Fig. 3. Example 1: concentration fields, c, using $q_D = 2\times10^{-4}$ m/s at $\partial\Omega_1$; I.V. = 42 m^3 (**a**) coarse mesh (**b**) fine mesh and I.V. = 180 m^3 (**c**) coarse mesh (**d**) fine mesh. The boundary conditions shown in this picture are corresponding to $\partial\Omega_1$ and $\partial\Omega_3$ of the mass balance equation (12). For the coarse mesh, the number of element is 3180 and $h = 2.01$ m. For the fine mesh, the number of element is 14024 and $h = 1.10$ m.

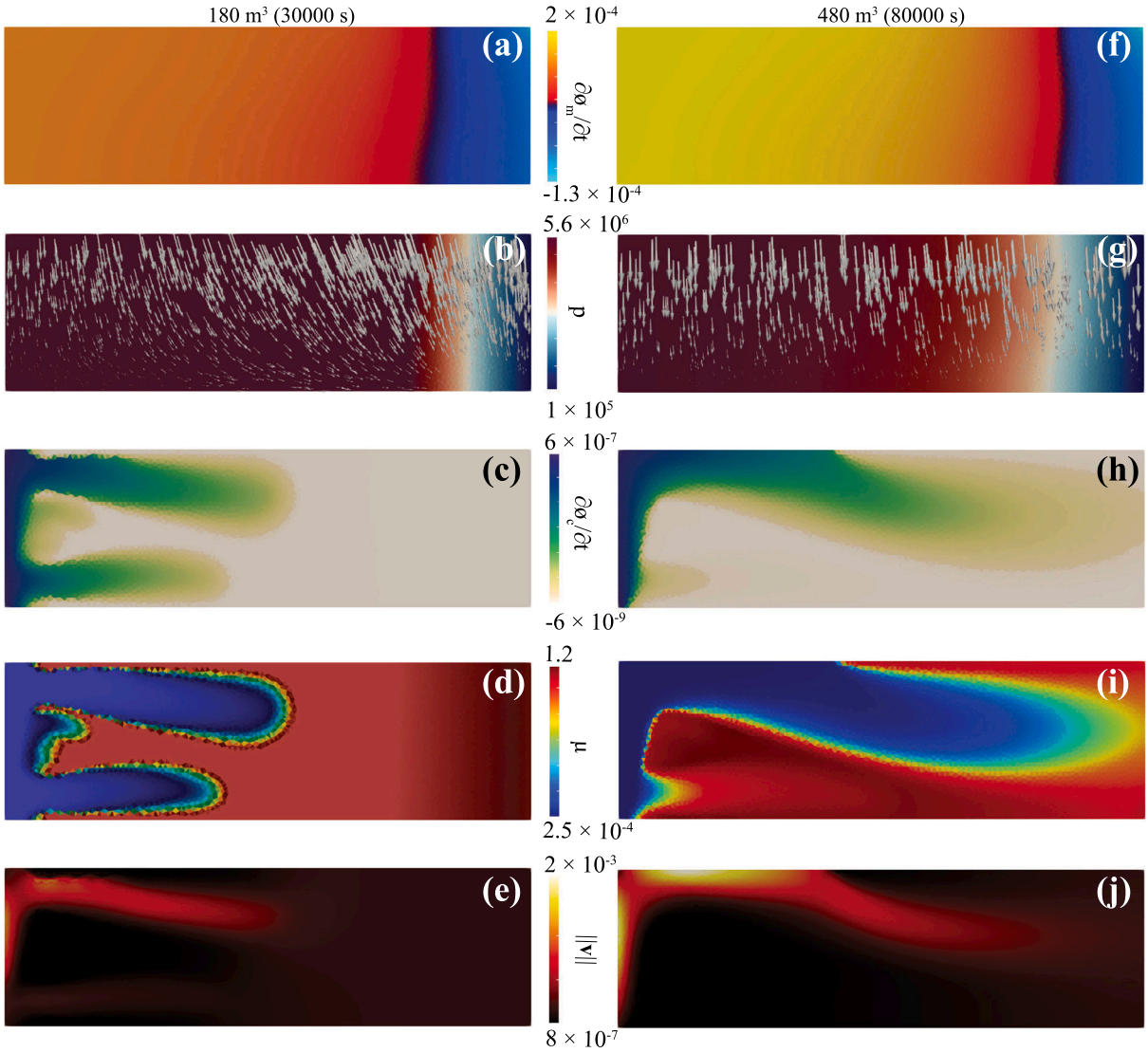

Fig. 4. Example 1: using $q_D = 2\times10^{-4}$ m/s at $\partial\Omega_1$; I.V. = 42 m^3: (**a**) the rate of change of porosity according to mechanics deformation, $\frac{\partial\phi_m}{\partial t}$, see (23), (**b**) the fluid pressure, p, in surface and the displacement, $\boldsymbol{u}$, in gray arrows, (**c**) the rate of change of porosity according to calcite dissolution/precipitation, $\frac{\partial\phi_c}{\partial t}$, see (24), (**d**) the fluid viscosity, μ, and (**e**) the magnitude of the fluid velocity, $\|\boldsymbol{q}\|$. I.V. = 480 m^3: (**f**) $\frac{\partial\phi_m}{\partial t}$, (**g**) p in surface and $\boldsymbol{u}$ in gray arrows, (**h**) $\frac{\partial\phi_c}{\partial t}$, (**i**) μ, and (**j**) $\|\boldsymbol{q}\|$. Note that the magnitude of $\boldsymbol{u}$ is from 0.0 to 3.0×10^{-2}, and the trend of the results of the $q_D = 1\times10^{-4}$ m/s at $\partial\Omega_1$ case are similar.

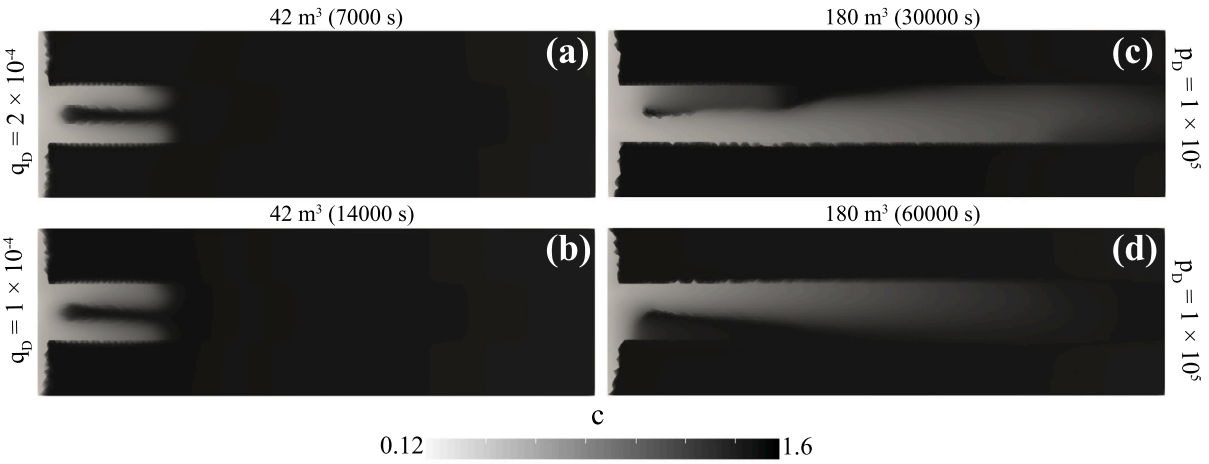

Fig. 5. Example 2: concentration fields, c; I.V. = 42 m^3 using (**a**) $q_D = 2\times10^{-4}$ m/s at $\partial\Omega_1$ and (**b**) $q_D = 1\times10^{-4}$ m/s at $\partial\Omega_1$; and I.V. = 180 m^3 using (**c**) $q_D = 2\times10^{-4}$ m/s at $\partial\Omega_1$ and (**d**) $q_D = 1\times10^{-4}$ m/s at $\partial\Omega_1$. The boundary conditions shown in this picture are corresponding to $\partial\Omega_1$ and $\partial\Omega_3$ of the mass balance equation (12).

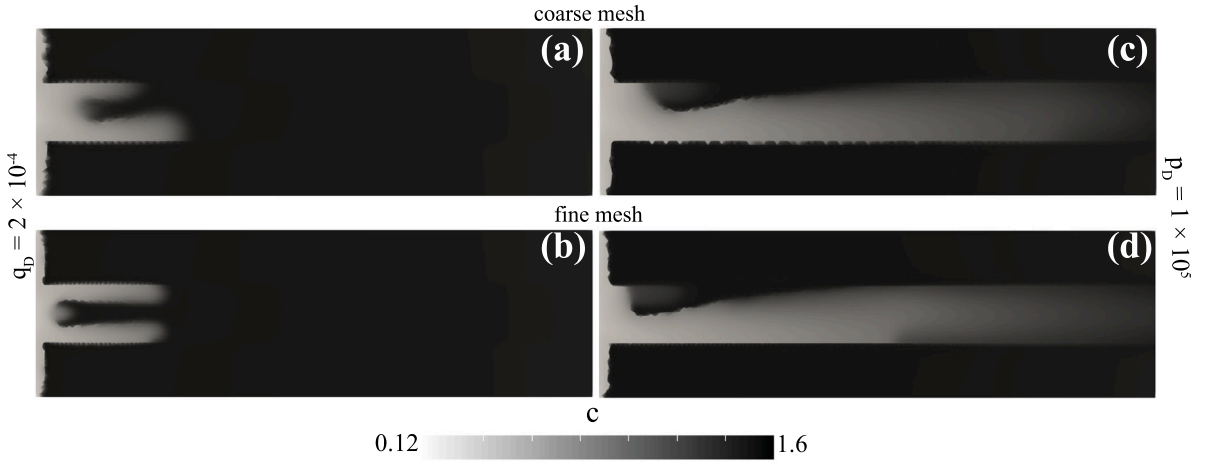

Fig. 6. Example 2: concentration fields, c, using $q_D = 2\times10^{-4}$ m/s at $\partial\Omega_1$; I.V. = 42 m^3 (**a**) coarse mesh (**b**) fine mesh and I.V. = 180 m^3 (**c**) coarse mesh (**d**) fine mesh. The boundary conditions shown in this picture are corresponding to $\partial\Omega_1$ and $\partial\Omega_3$ of the mass balance equation (12). For the coarse mesh, the number of element is 3180 and $h = 2.01$ m. For the fine mesh, the number of element is 14024 and $h = 1.10$ m.

4.2. Example 2

In the second example, we consider three layers ($\Omega_{500} = [0, 100]\times[10, 20]$, $\Omega_{501} = [0, 100]\times[20, 30]$, and $\Omega_{502} = [0, 100]\times[0, 10]$) as the computational domain. See Fig. 1b. In Ω_{500}, we set $\boldsymbol{k} = 8.8\times10^{-10}\mathbf{I}$ m^2, while $\boldsymbol{k} = 8.8\times10^{-11}\mathbf{I}$ m^2 in Ω_{501} and Ω_{502}. Thus, in this case, the top Ω_{501} and bottom Ω_{502} layers have one order of magnitude of $\boldsymbol{k}$ less than that of the middle layer Ω_{500}. All other rock and fluid parameters are the same as in the first example.

The concentration field c for two different injection scenarios (as discussed in example 1) for the three-layer porous medium are presented in Fig. 5. Unlike the single-layer porous medium, even though the concentration fields at the early time are similar between the high, $q_D = 2\times10^{-4}$ m/s, and low, $q_D = 1\times10^{-4}$ m/s, injection rates, the progression of concentration field is different at the later time. It appears that the dynamic of the coupled processes controlled by the injection rate can impact the development of the dominant finger in the middle layer. Note that since the top and bottom layers, Ω_{501} and Ω_{502}, have lower permeability than the middle layer, Ω_{500}, the flow mainly goes through the middle layer. Similar to the previous example, one of the two initial fingers becomes the main path connecting the inlet and the outlet boundaries.

We also perform the simulation using different mesh sizes for this example. Our results are shown in Fig. 6 for the c field and Fig. 7 for the c contour. Again, we note that the number of element is 3180 and $h = 2.01$ m for the coarse mesh, and the number of element is 14024 and $h = 1.10$ m for the fine mesh. Initially the coarser mesh results in slightly different size of fingers (Figs. 5a, 6a, 6b). The c result, however, converges to the similar behavior when we decrease the mesh size (h) (Figs. 7).

In Fig. 8, the behavior of the concentration and velocity fields, together with temporal porosity alteration ($\frac{\partial\phi_c}{\partial t}$), are illustrated for both injection scenarios. As mentioned earlier, due to the difference of viscosity (μ) between that of the injected c and the in-situ c, two fingers developed at the beginning, see Fig. 8a and e. For the high injection rate, the top finger, however, disappeared while the bottom finger progresses until it reaches the outlet $\partial\Omega_3$, see Figs. 8b–d. One could see that the reaction front shown by $\frac{\partial\phi_c}{\partial t}$ progresses similarly to the concentration front shown by the black contours. Besides, as the concentration field develops, the change in μ enhances the flow channeling illustrated by velocity arrows.

For the low injection rate case shown in Fig. 8e–h, the development of the concentration field is dissimilar to that of the high injection rate case as the top finger becomes a preferable path instead of the bottom one. Note that the dissolution and precipitation are shown in Fig. 8 are a combined effect of injecting water that is unsaturated with respect to calcite and fluid pressure changes. It is clear that the majority of the dissolution occurs due to the transport of the injected water in

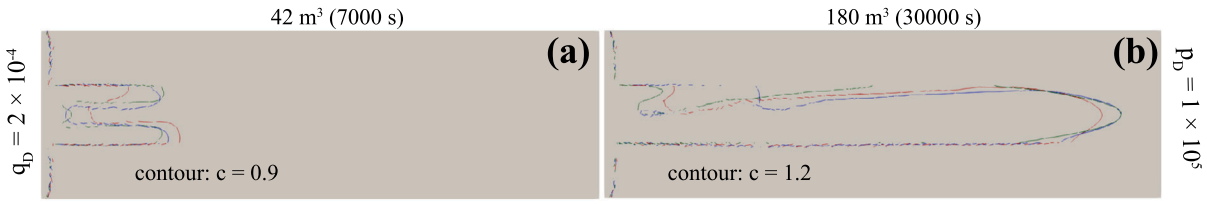

Fig. 7. Example 2: concentration contours, c, using $q_D = 2\times10^{-4}$ m/s at $\partial\Omega_1$; (**a**) I.V. = 42 m³ and (**b**) I.V. = 180 m³ for three meshes — number of element is 3180, $h = 2.01$ m, (in red), number of element is 7852, $h = 1.47$ m, (in blue), and number of element is 14024, $h = 1.10$ m, (in green). The boundary conditions shown in this picture are corresponding to $\partial\Omega_1$ and $\partial\Omega_3$ of the mass balance equation (12). (For interpretation of the references to color in this figure legend, the reader is referred to the web version of this article.)

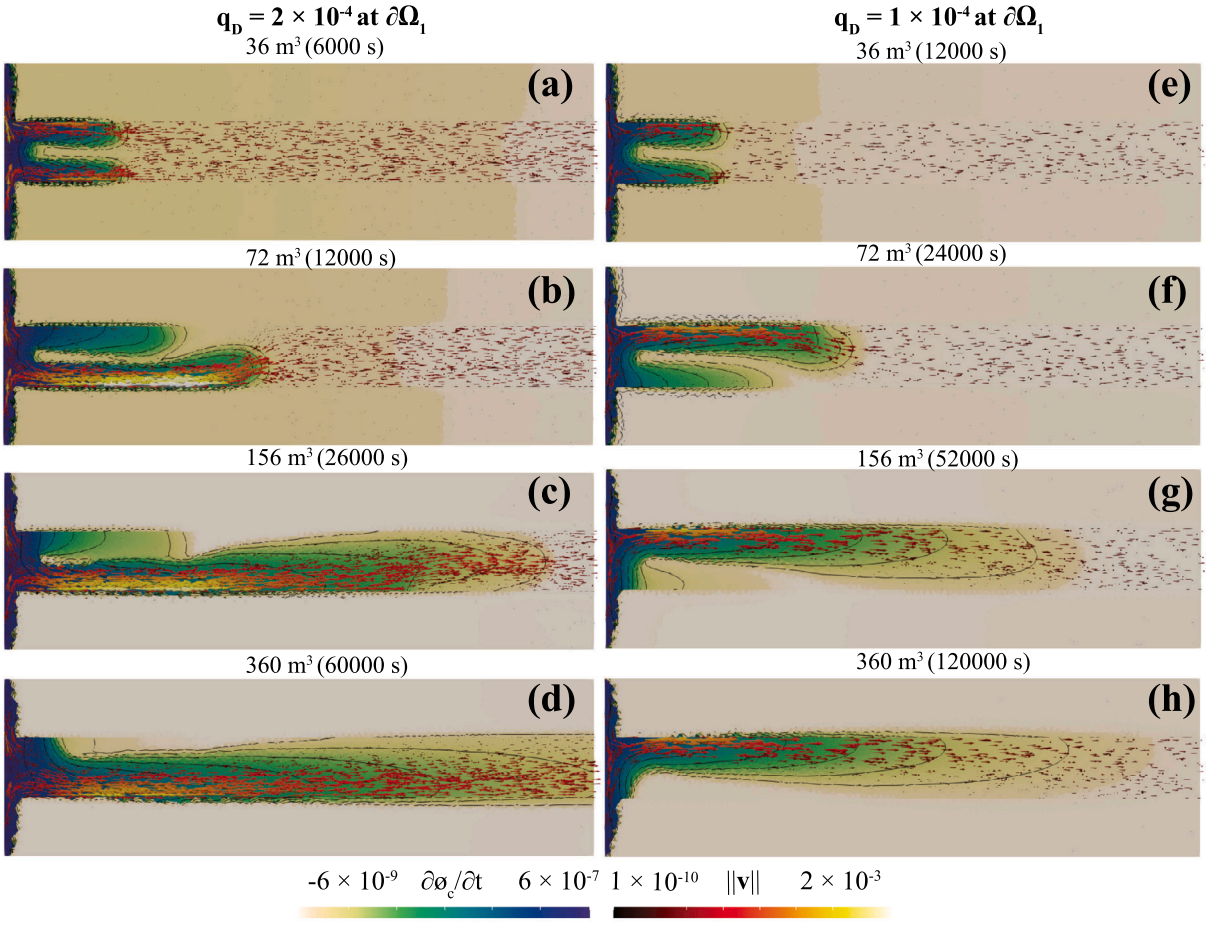

Fig. 8. Example 2: the results of the rate of change of porosity according to calcite dissolution/precipitation ($\frac{\partial\phi_c}{\partial t}$) shown in surface plot, concentration (c), shown in black contour (10 contours ranging from 0.12 to 1.6), and the fluid velocity ($\boldsymbol{q}$) shown in arrows with $q_D = 2\times10^{-4}$ m/s at $\partial\Omega_1$; (**a**) I.V. = 36 m³ (t = 6000 s), (**b**) I.V. = 72 m³ (t = 12000 s), (**c**) I.V. = 156 m³ (t = 26000 s), and (**d**) I.V. = 360 m³ (t = 60000 s), and with $q_D = 1\times10^{-4}$ m/s at $\partial\Omega_1$; (**e**) I.V. = 36 m³ (t = 1200 s), (**f**) I.V. = 72 m³ (t = 24000 s), (**g**) I.V. = 156 m³ (t = 32000 s), and (**h**) I.V. = 360 m³ (t = 120000 s).

the porous domain. For the animated version of Fig. 8, please refer to Videos 1 and 2. These videos represent the flow and concentration field as well as $\frac{\partial\phi_c}{\partial t}$ and illustrate the applicability of the presented coupled model for heterogeneous porous media.

Importantly, this example has illustrated the capability of our proposed method – which is equipped with the EG method – for handling discontinuous material properties across different layers and the sharp interface of the concentration species. Moreover, we have again observed the expected physical and chemical phenomena, including solid deformation, viscous fingering, and dissolution/precipitation.

4.3. Example 3

In the given computational domain $\Omega_{500} = [0, 100]\times[0, 30]$, we investigate the setup with the heterogeneous $\boldsymbol{k}$ values as shown in Fig. 1c. A random field generator (Nick et al., 2009) is utilized to generate a heterogeneous permeability field with a given mean permeability of $\boldsymbol{k} = 1\times10^{-10}\mathbf{I}$ m², variance of 0.5, and correlation lengths in x- and y-direction of 5 and 1 m, respectively. The heterogeneous permeability field varies in two orders of magnitude. All other physical parameters are the same as in the previous examples.

Here, we focus on the interplay between the heterogeneous permeability and the HMC coupled processes. Similar to the previous examples, two different injection rates are applied. In Fig. 9, the concentration fields are illustrated for two different injection rates at different injected fluid volumes (I.V. = 42 m³ and I.V. = 180 m³). Unlike the two previous examples, the preferential paths are established not only because of the flow instability resulting from the μ difference but also due to the high $\boldsymbol{k}$ channels inherited from the nature of heterogeneous porous media. During the early time, the concentration field of the high, $q_D = 2\times10^{-4}$ m/s, and low, $q_D = 1\times10^{-4}$ m/s, injection

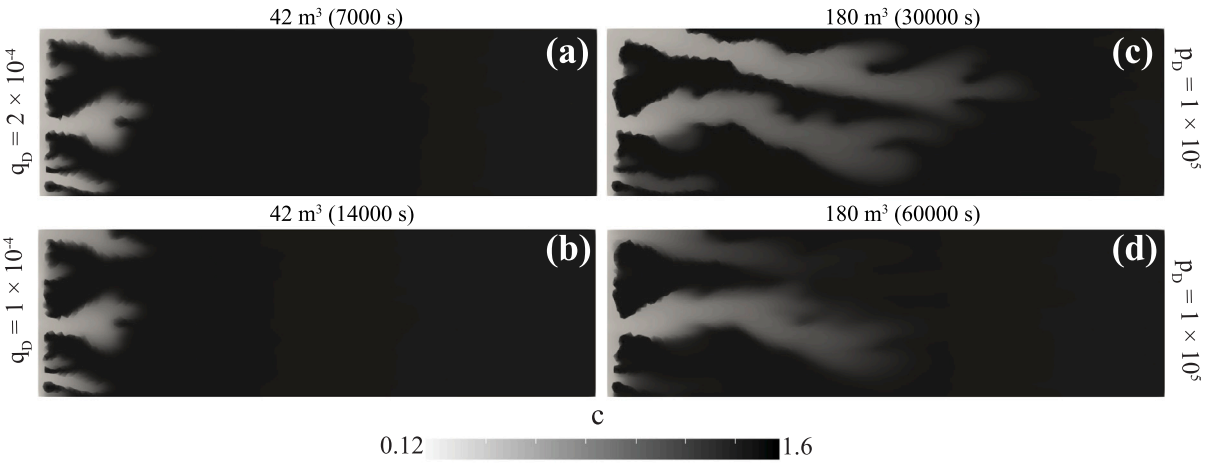

Fig. 9. Example 3: concentration fields, c; I.V. = 42 m^3 using (**a**) $q_D = 2 \times 10^{-4}$ m/s at $\partial\Omega_1$ and (**b**) $q_D = 1 \times 10^{-4}$ m/s at $\partial\Omega_1$; and I.V. = 180 m^3 using (**c**) $q_D = 2 \times 10^{-4}$ m/s at $\partial\Omega_1$ and (**d**) $q_D = 1 \times 10^{-4}$ m/s at $\partial\Omega_1$. The boundary conditions shown in this picture are corresponding to $\partial\Omega_1$ and $\partial\Omega_3$ of the mass balance equation (12).

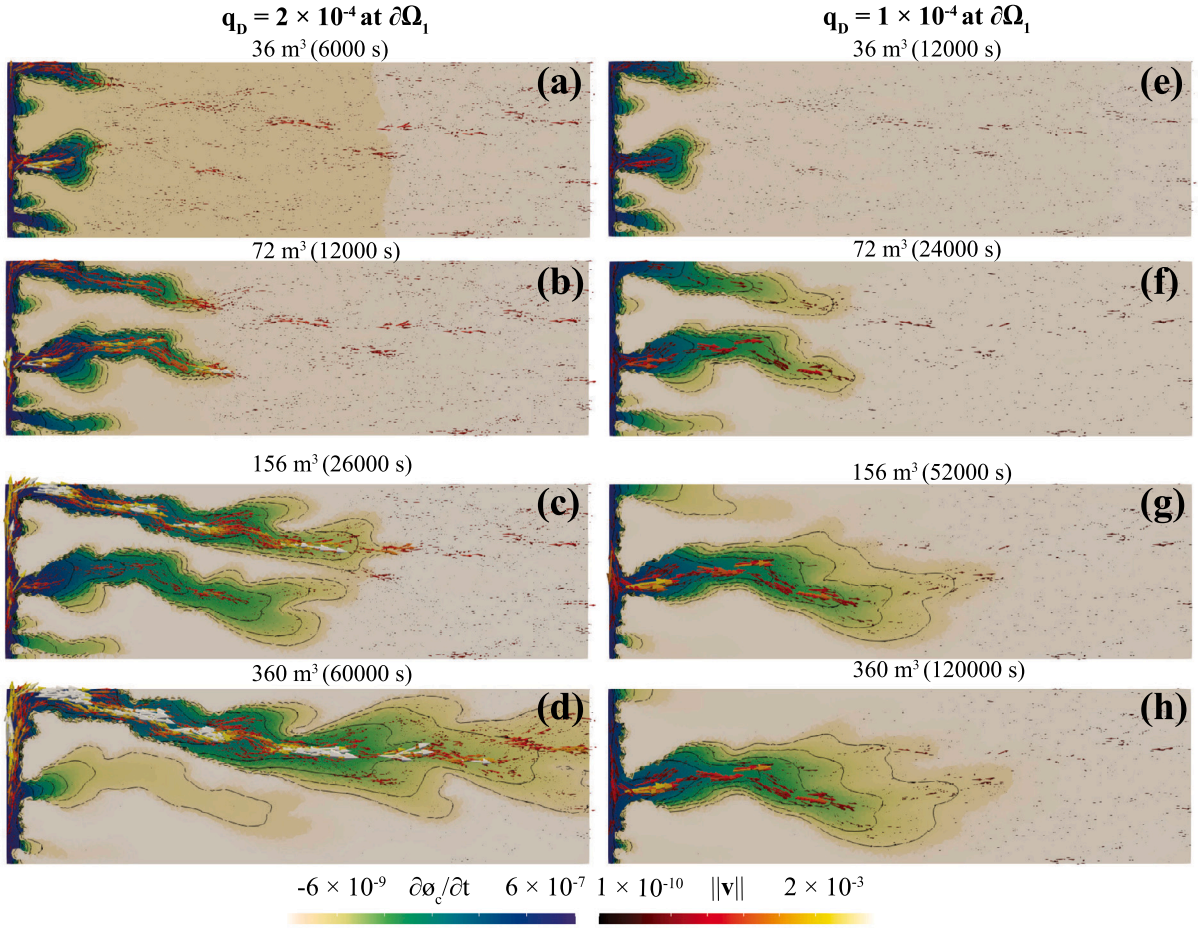

Fig. 10. Example 3: the results of the rate of change of porosity according to calcite dissolution/precipitation ($\frac{\partial \phi_c}{\partial t}$) shown in surface plot, concentration (c), shown in black contour (10 contours ranging from 0.12 to 1.6), and the fluid velocity (q) shown in arrows with $q_D = 2 \times 10^{-4}$ m/s at $\partial\Omega_1$; (**a**) I.V. = 36 m^3 (t = 6000 s), (**b**) I.V. = 72 m^3 (t = 12000 s), (**c**) I.V. = 156 m^3 (t = 26000 s), and (**d**) I.V. = 360 m^3 (t = 60000 s), and with $q_D = 1 \times 10^{-4}$ m/s at $\partial\Omega_1$; (**e**) I.V. = 36 m^3 (t = 1200 s), (**f**) I.V. = 72 m^3 (t = 24000 s), (**g**) I.V. = 156 m^3 (t = 32000 s), and (**h**) I.V. = 360 m^3 (t = 120000 s).

rate cases are similar, see Fig. 9a–b. The results of the concentration with the effects from the reaction are different at a later time (see Fig. 9c–d). During the early time for both cases, the developed fingers follow the high permeable paths. At a later time, however, the results of the two scenarios are very different. For the high injection rate case, the top finger continues developing while the middle and the bottom fingers disappear. The result of the low injection rate case, however, shows that the top and the bottom fingers perish while the middle finger progresses.

Fig. 10 provides further insight into the reactive flow dynamics. It shows for both injection scenarios how the reaction fronts and flow fields evolve in time. As mentioned earlier, all the initial fingers at

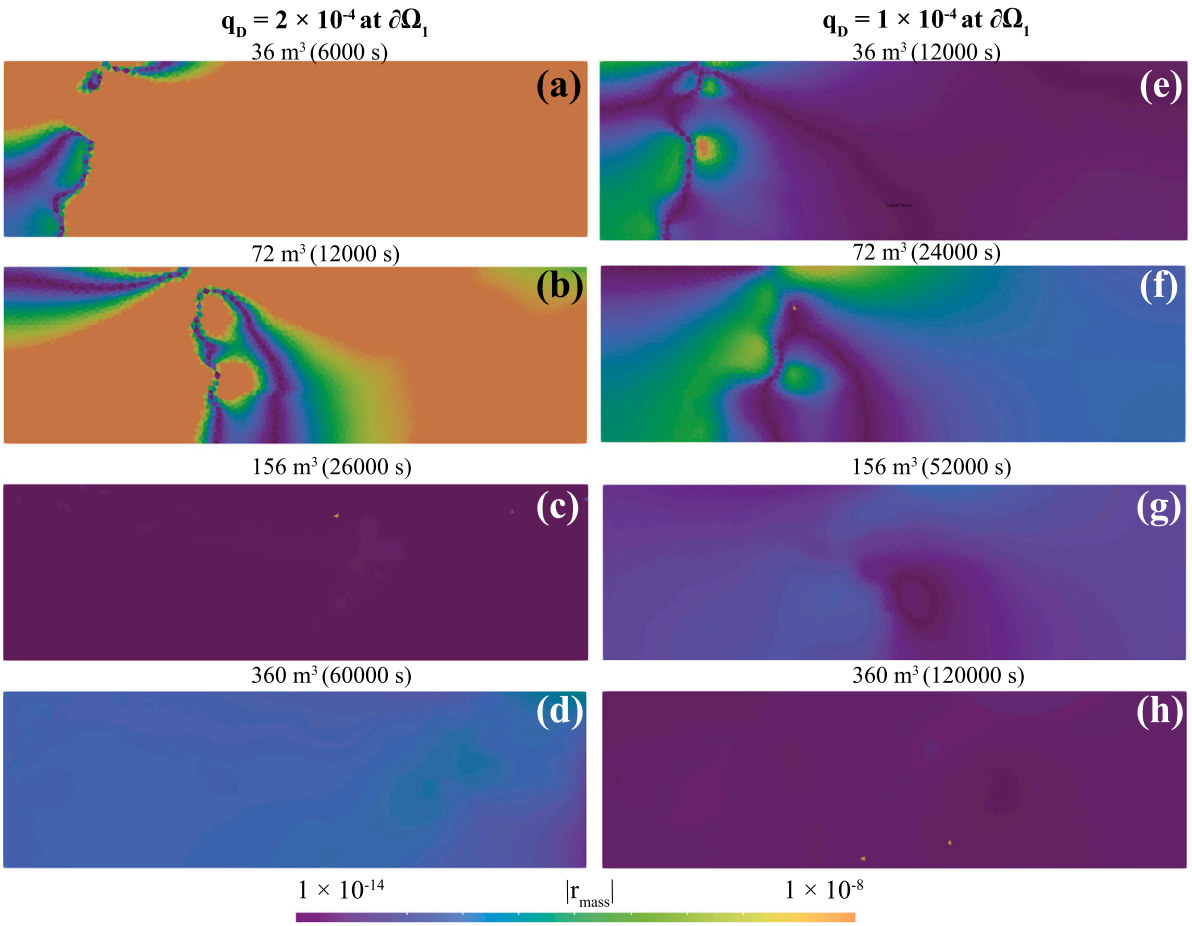

Fig. 11. Example 3: the illustration of the local mass conservative property with $q_D = 2 \times 10^{-4}$ m/s at $\partial\Omega_1$; **(a)** I.V. = 36 m³ (t = 6000 s), **(b)** I.V. = 72 m³ (t = 12000 s), **(c)** I.V. = 156 m³ (t = 26000 s), and **(d)** I.V. = 360 m³ (t = 60000 s), and with $q_D = 1 \times 10^{-4}$ m/s at $\partial\Omega_1$; **(e)** I.V. = 36 m³ (t = 1200 s), **(f)** I.V. = 72 m³ (t = 24000 s), **(g)** I.V. = 156 m³ (t = 32000 s), and **(h)** I.V. = 360 m³ (t = 120000 s).

the beginning vanish except one that reaches the outlet $\partial\Omega_3$. The flow velocity field variations in time depict the emergence of the dominant finger. Note that the magnitude of the mechanical deformation is higher than that of the calcite dissolution/precipitation and similar to what was observed in example 1. Therefore changes in porosity due to chemical reaction have a second-order effect on permeability compared to that of induced by the mechanical deformation. Videos 3 and 4 representing the flow and concentration field as well as $\frac{\partial \phi_c}{\partial t}$ illustrate the applicability of the presented coupled model for heterogeneous porous media.

Next, we investigate the local mass conservation property of the proposed framework in the heterogeneous domain. The local mass conservation of each cell at each time step, $\mathrm{r}^{\mathrm{n}}_{\mathrm{mass}}$, is calculated by

$$\mathrm{r}^{\mathrm{n}}_{\mathrm{mass}} := \int_T \left(\frac{1}{M} + \frac{\alpha^2}{K}\right)\frac{p^n - p^{n-1}}{\Delta t^n} + \frac{\alpha}{K}\frac{\sigma_v^n - \sigma_v^{n-1}}{\Delta t^n} + \frac{\hat{\phi_c}^n - \phi_c^{n-1}}{\Delta t^n} dV + \sum_{e\in\mathcal{E}_h}\int_e \bar{q}^n \cdot \mathbf{n}|_{\mathrm{e}}\, dS, \tag{59}$$

and the discrete numerical flux approximated by BDM, $\bar{q}^n \cdot \mathbf{n}|_{\mathrm{e}}$, is defined by

$$\bar{q}^n := q_h^n \quad \forall T \in \mathcal{T}_h, \tag{60}$$

$$\bar{q}^n \cdot \mathbf{n}|_{\mathrm{e}} := -q_D \quad \forall e \in \mathcal{E}_h^{N,m}, \tag{61}$$

$$\bar{q}^n \cdot \mathbf{n}|_{\mathrm{e}} := -q_h^n \cdot \mathbf{n} \quad \forall e \in \mathcal{E}_h^{D,m}. \tag{62}$$

In Fig. 11, the values of $\mathrm{r}^{\mathrm{n}}_{\mathrm{mass}}$ are illustrated for each case and time. One could see that the magnitude of $\mathrm{r}^{\mathrm{n}}_{\mathrm{mass}}$ is always less than 1×10^{-5}, which is the tolerance set for the fixed-stress loop, see Algorithm 1; therefore, the framework is locally mass conservative. We note that the high injection rate case tends to the higher value of the magnitude of $\mathrm{r}^{\mathrm{n}}_{\mathrm{mass}}$ than that of the low injection rate case.

4.4. Example 4

Lastly, we investigate the performance of the proposed framework when the permeability field is anisotropic, and the grid is unstructured, as shown in Fig. 1d. In the computational domain $\Omega_{500} = [0, 100] \times [0, 30]$, see Fig. 1a, we consider the anisotropic permeability field to emphasize the capability of our proposed algorithm. The permeability tensor of this example is defined as follows:

$$\boldsymbol{k} := \begin{bmatrix} k_{xx} & 0.0 \\ 0.0 & 0.1k_{xx} \end{bmatrix}, \tag{63}$$

where $k_{xx} = 8.8 \times 10^{-10}$ m² and all other parameters are similar to all other cases.

Fig. 12 shows the reactive flow dynamics and the residual of mass. We observe that the flow in the horizontal direction dominates the flow in the vertical direction since the permeability in the horizontal direction is ten times higher than that of the vertical direction. Fig. 12d–f illustrate that the proposed framework is locally mass conservative as the residual of mass values are always less than 1×10^{-5}, which is the tolerance set for the fixed-stress loop.

4.5. Discussion

The main observations of the foregoing numerical examples can be summarized as follows:

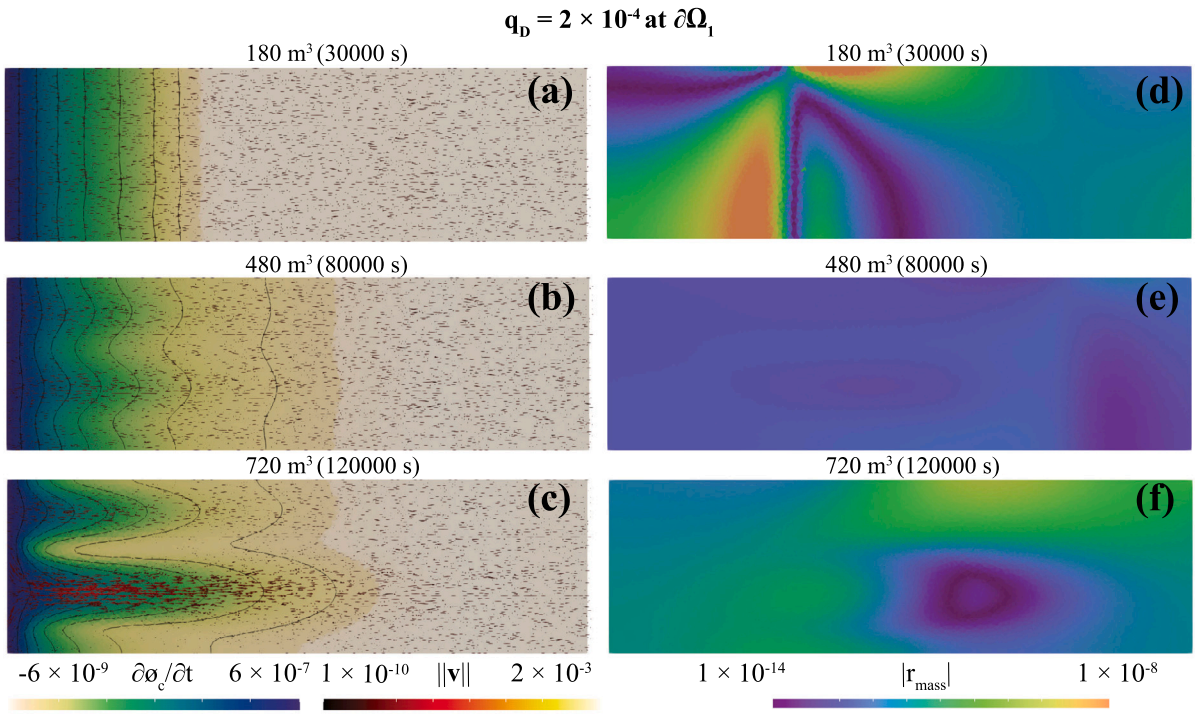

Fig. 12. Example 4: the results of the rate of change of porosity according to calcite dissolution/precipitation ($\frac{\partial \phi_c}{\partial t}$) shown in surface plot, concentration (c), shown in black contour (10 contours ranging from 0.12 to 1.6), and the fluid velocity ($\boldsymbol{q}$) shown in arrows with $q_D = 2 \times 10^{-4}$ m/s at $\partial\Omega_i$; (**a**) I.V. = 180 m^3 (t = 30000 s), (**b**) I.V. = 480 m^3 (t = 80000 s), and (**c**) I.V. = 720 m^3 (t = 120000 s), and the local mass conservative property; (**d**) I.V. = 180 m^3 (t = 30000 s), (**e**) I.V. = 480 m^3 (t = 80000 s), and (**f**) I.V. = 720 m^3 (t = 120000 s).

1. The injection rate supplied at the inlet boundary is critical in defining flow behavior. The preferential flow paths developed through time are significantly different with different injection rates. Besides, the injection flow rate also controls the development of the advection and reaction fronts.
2. Using the applied set of the input parameters resulted in a more noticeable mechanical effect on the change in ϕ (and subsequently in $\boldsymbol{k}$) compared to that of the calcite dissolution/precipitation effect. We note that this observation could vary with different sets of input parameters and required to be further investigated. The change in μ resulted from the change in c is significant, resulting in the development of preferential flow paths.
3. The results of both homogeneous and heterogeneous as well as isotropic and anisotropic permeability field show that our framework preserves mass locally. This property is essential for the coupled HMC system.

In terms of computational efficiency, it is noted that the iteration number for the fixed-stress iteration was around three (four for the example 3) at the initial time stage, but it only required two iterations for the rest of the time for all the presented examples. For all examples, we have 31934, 23818, 7852, 11910 degrees of freedom for the displacement, flux, pressure, and concentration fields, respectively. The computational time was around 4.78×10^{-5} second per degrees of freedom per each time step. All simulations were computed on XeonE5_2650v4 with a single thread.

5. Conclusion

This paper has presented a mixed finite element framework for coupled hydro-mechanical–chemical processes in heterogeneous porous media. The main advantage of the proposed framework is its relatively affordable cost to attain local conservation regardless of material anisotropy, thanks particularly to the use of the EG method. Through several numerical examples, we have demonstrated the performance and capabilities of the proposed framework with a focus on local conservation. The numerical results have highlighted how the overall behavior is influenced by different processes, including solid deformation, calcite dissolution, and fluid viscosity alteration. The developed numerical model can provide insight into how the interactions among HMC processes and heterogeneity manifest themselves at a larger scale. Future work includes an extension of the modeling framework to coupled thermo-hydro-mechanical–chemical processes in heterogeneous and/or fractured porous media.

Computer code availability

The scripts used to produce these results are available at https://github.com/teeratornk/supplementary_scripts_for_HMC_manuscript. The main dependencies are Numpy ≥ 1.16.5, FEniCS (https://fenicsproject.org) ≥ 2018.1.0 with PETSc (https://www.mcs.anl.gov/petsc) ≥ 3.10.5 and petsc4py ≥ 3.10, and multiphenics (https://mathlab.sissa.it/multiphenics) ≥ 0.2.0.

CRediT authorship contribution statement

T. Kadeethum: Conceptualization, Formal analysis, Software, Validation, Writing - original draft, Writing - review & editing. **S. Lee:** Conceptualization, Formal analysis, Supervision, Validation, Writing - review & editing. **F. Ballarin:** Conceptualization, Formal analysis, Software, Supervision, Validation, Writing - review & editing. **J. Choo:** Conceptualization, Formal analysis, Supervision, Writing - review & editing. **H.M. Nick:** Conceptualization, Funding acquisition, Supervision, Writing - review & editing.

Declaration of competing interest

The authors declare that they have no known competing financial interests or personal relationships that could have appeared to influence the work reported in this paper.

Acknowledgments

This research has received financial support from the Danish Hydrocarbon Research and Technology Centre under the Advanced Water Flooding program. The computational results in this work have been produced by the multiphenics library (Ballarin and Rozza, 2019), which is an extension of FEniCS (Alnaes et al., 2015) for multiphysics problems. We acknowledge the developers of and contributors to these libraries. TK also thanks the 2019 Computers & Geosciences Research grant for the additional support. SL is supported by the National Science Foundation under Grant No. NSF DMS-1913016. FB thanks Horizon 2020 Program for Grant H2020 ERC CoG 2015 AROMA-CFD project 681447 that supported the development of multiphenics. JC acknowledges support from the Research Grants Council of Hong Kong under Project 27205918.

References

Aavatsmark, Ivar, 2002. An introduction to multipoint flux approximations for quadrilateral grids. Comput. Geosci. 6 (3), 405–432.

Abou-Kassem, J., Islam, M., Farouq-Ali, S., 2013. Petroleum Reservoir Simulations. Elsevier.

Ahkami, M., Parmigiani, A., Di Palma, P., Saar, M., Kong, X., 2020. A lattice-Boltzmann study of permeability-porosity relationships and mineral precipitation patterns in fractured porous media. Comput. Geosci. 1–18.

Akinfenwa, O., Jator, S., Yao, N., 2013. Continuous block backward differentiation formula for solving stiff ordinary differential equations. Comput. Math. Appl. 65 (7), 996–1005.

Alnaes, M., Blechta, J., Hake, J., Johansson, A., Kehlet, B., Logg, A., Richardson, C., Ring, J., Rognes, M., Wells, G., 2015. The FEniCS project version 1.5. Arch. Numer. Softw. 3 (100).

Araya, R., Behrens, E., Rodriguez, R., 2005. An adaptive stabilized finite element scheme for the advection–reaction–diffusion equation. Appl. Numer. Math. 54 (3–4), 491–503.

Balay, S., Abhyankar, S., Adams, M., Brown, J., Brune, P., Buschelman, K., Dalcin, L., Dener, A., Eijkhout, V., Gropp, W., Kaushik, D., Knepley, M., May, D., McInnes, L., Mills, R., Munson, T., Rupp, K., Sanan, P., Smith, B., Zampini, S., Zhang, H., Zhang, H., 2018. PETSc Users Manual. Tech. Rep. ANL-95/11 - Revision 3.10, Argonne National Laboratory, URL http://www.mcs.anl.gov/petsc.

Ballarin, F., Rozza, G., 2019. Multiphenics - easy prototyping of multiphysics problems in FEniCS. URL https://mathlab.sissa.it/multiphenics.

Bijeljic, B., Blunt, M., 2007. Pore-scale modeling of in porous media. Water Resour. Res. 43 (12).

Biot, M., 1941. General theory of three-dimensional consolidation. J. Appl. Phys. 12 (2), 155–164.

Biot, M., Willis, D., 1957. The elastic coefficients of the theory of consolidation. J. Appl. Mech. 15, 594–601.

Bonito, A., Guermond, J., Popov, B., 2014. Stability analysis of explicit entropy viscosity methods for non-linear scalar conservation equations. Math. Comp. 83 (287), 1039–1062.

Borja, R.I., Choo, J., 2016. Cam-Clay plasticity, Part VIII: A constitutive framework for porous materials with evolving internal structure. Comput. Methods Appl. Mech. Engrg. 309, 653–679.

Brezzi, F., Bristeau, M., Franca, L., Mallet, M., Roge, G., 1992. A relationship between stabilized finite element methods and the Galerkin method with bubble functions. Comput. Methods Appl. Mech. Engrg. 96 (1), 117–129.

Brezzi, F., Fortin, M., 2012. Mixed and Hybrid Finite Element Methods, volume 15. Springer Science & Business Media.

Chaudhuri, A., Rajaram, H., Viswanathan, H., 2013. Early-stage hypogene karstification in a mountain hydrologic system: A coupled thermohydrochemical model incorporating buoyant convection. Water Resour. Res. 49 (9), 5880–5899.

Chen, Z., 2007. Reservoir Simulation: mathematical Techniques in Oil Recovery, volume 77. Siam.

Chen, Z., Huan, G., Ma, Y., 2006. Computational Methods for Multiphase Flows in Porous Media, volume 2. Siam.

Choi, W., Lee, S., 2020. Optimal error estimate of elliptic problems with Dirac sources for discontinuous and enriched Galerkin methods. Appl. Numer. Math. 150, 76–104. http://dx.doi.org/10.1016/j.apnum.2019.09.010, URL http://www.sciencedirect.com/science/article/pii/S0168927419302491.

Choo, J., 2018. Large deformation poromechanics with local mass conservation: An enriched Galerkin finite element framework. Internat. J. Numer. Methods Engrg. 116 (1), 66–90.

Choo, J., 2019. Stabilized ntinuous/enriched Galerkin formulations for locally mass conservative poromechanics. Comput. Methods Appl. Mech. Engrg. 357, 112568.

Choo, J., Lee, S., 2018. Enriched Galerkin finite elements for coupled poromechanics with local mass conservation. Comput. Methods Appl. Mech. Engrg. 341, 311–332.

Choo, J., Sun, W., 2018. Cracking and damage from crystallization in pores: Coupled chemo-hydro-mechanics and phase-field modeling. Comput. Methods Appl. Mech. Engrg. 335, 347–349.

Choo, J., White, J., Borja, R.I., 2016. Hydromechanical modeling of unsaturated flow in double porosity media. Int. J. Geomech. 16 (6), D4016002.

Courant, R., Friedrichs, K., Lewy, H., 1967. On the partial difference equations of mathematical physics. IBM J. Res. Dev. 11 (2), 215–234.

Coussy, O., 2004. Poromechanics. John Wiley & Sons.

Dana, S., Ganis, B., Wheeler, M., 2018. A multiscale fixed stress split iterative scheme for coupled flow and poromechanics in deep subsurface reservoirs. J. Comput. Phys. 352, 1–22.

Dana, S., Wheeler, M., 2018. Convergence analysis of two-grid fixed stress split iterative scheme for coupled flow and deformation in heterogeneous poroelastic media. Comput. Methods Appl. Mech. Engrg. 341, 788–806.

Dormand, J., Prince, P., 1980. A family of embedded Runge-Kutta formulae. J. Comput. Appl. Math. 6 (1), 19–26.

Du, J., Wong, R., 2007. Application of strain-induced permeability model in a coupled geomechanics-reservoir simulator. J. Can. Pet. Technol. 46 (12), 55–61.

Ern, A., Stephansen, A., 2008. A posteriori energy-norm error estimates for advection-diffusion equations approximated by weighted interior penalty methods. J. Comput. Math. 488–510.

Ern, A., Stephansen, A., Zunino, P., 2009. A discontinuous Galerkin method with weighted averages for advection-diffusion equations with locally small and anisotropic diffusivity. IMA J. Numer. Anal. 29 (2), 235–256.

Ferronato, M., Castelletto, N., Gambolati, G., 2010. A fully coupled 3-D mixed finite element model of biot consolidation. J. Comput. Phys. 229 (12), 4813–4830.

Grolimund, D., Elimelech, M., Borkovec, M., 2001. Aggregation and deposition kinetics of mobile colloidal particles in natural porous media. Colloids Surf. A 191 (1–2), 179–188.

Guermond, J., Popov, B., Tomas, I., 2019. Invariant domain preserving discretization-independent schemes and convex limiting for hyperbolic systems. Comput. Methods Appl. Mech. Engrg. 347, 143–175.

Haga, J., Osnes, H., Langtangen, H., 2012. On the causes of pressure oscillations in low permeable and low compressible porous media. Int. J. Numer. Anal. Methods Geomech. 36 (12), 1507–1522.

Harari, I., Hughes, T., 1994. Stabilized finite element methods for steady advection—diffusion with production. Comput. Methods Appl. Mech. Engrg. 115 (1–2), 165–191.

Hu, M., Hueckel, T., 2013. Environmentally enhanced crack propagation in a chemically degrading isotropic shale. Géotechnique 63 (4), 313–321.

Ibrahim, Z., Othman, K., Suleiman, M., 2007. Implicit r-point block backward differentiation formula for solving first-order stiff ODEs. Appl. Math. Comput. 186 (1), 558–565.

Jaeger, J., Cook, Neville G., Zimmerman, R., 2009. Fundamentals of Rock Mechanics. John Wiley & Sons.

Jha, B., Juanes, R., 2007. A locally conservative finite element framework for the simulation of coupled flow and reservoir geomechanics. Acta Geotech. 2 (3), 139–153.

Kadeethum, T., Ballarin, F., Bouklas, N., 2021a. Non-intrusive reduced order modeling of poroelasticity of heterogeneous media based on a discontinuous Galerkin approximation. arXiv preprint arXiv:2101.11810.

Kadeethum, T., Lee, S., Nick, H., 2020a. Finite element solvers for Biot's poroelasticity equations in porous media. Math. Geosci. 1–39.

Kadeethum, T., Nick, H., Lee, S., Ballarin, F., 2020b. Flow in porous media with low dimensional fractures by employing enriched Galerkin method. Adv. Water Resour..

Kadeethum, T., Nick, H., Lee, S., Ballarin, F., 2021b. Enriched Galerkin discretization for modeling poroelasticity and permeability alteration in heterogeneous porous media. J. Comput. Phys. 110030.

Kadeethum, T., Nick, H., Lee, S., Richardson, C., Salimzadeh, S., Ballarin, F., 2019a. A novel enriched Galerkin method for modelling coupled flow and mechanical deformation in heterogeneous porous media. In: 53rd US Rock Mechanics/Geomechanics Symposium. American Rock Mechanics Association, New York, NY, USA.

Kadeethum, T., Salimzadeh, S., Nick, H., 2018. Investigation on the productivity behaviour in deformable heterogeneous fractured reservoirs. In: 2018 International Symposium on Energy Geotechnics.

Kadeethum, T., Salimzadeh, S., Nick, H., 2019b. An investigation of hydromechanical effect on well productivity in fractured porous media using full factorial experimental design. J. Petrol. Sci. Eng. 181, 106233.

Kadeethum, T., Salimzadeh, S., Nick, H., 2020c. Well productivity evaluation in deformable single-fracture media. Geothermics 87.

Kim, J., Tchelepi, H., Juanes, R., 2011. Stability and convergence of sequential methods for coupled flow and geomechanics: Fixed-stress and fixed-strain splits. Comput. Methods Appl. Mech. Engrg. 200 (13–16), 1591–1606.

Lee, S., Lee, Y., Wheeler, M., 2016. A locally conservative enriched Galerkin approximation and efficient solver for elliptic and parabolic problems. SIAM J. Sci. Comput. 38 (3), A1404–A1429.

Lee, S., Mikelic, A., Wheeler, M., Wick, T., 2018. Phase-field modeling of two phase fluid filled fractures in a poroelastic medium. Multiscale Model. Simul. 16 (4), 1542–1580.

Lee, S., Wheeler, M., 2017. Adaptive enriched Galerkin methods for miscible displacement problems with entropy residual stabilization. J. Comput. Phys. 331, 19–37.
Lee, S., Wheeler, M., 2018. Enriched Galerkin methods for two-phase flow in porous media with capillary pressure. J. Comput. Phys. 367, 65–86.
Lipnikov, K., Shashkov, M., Yotov, I., 2009. Local flux mimetic finite difference methods. Numer. Math. 112 (1), 115–152.
MacMinn, C., Dufresne, E., Wettlaufer, J., 2016. Large deformations of a soft porous material. Phys. Rev. A 5 (4), 1–30.
Masud, A., Khurram, R., 2004. A multiscale/stabilized finite element method for the advection–diffusion equation. Comput. Methods Appl. Mech. Engrg. 193 (21–22), 1997–2018.
Medetbekova, M., Christensen, H., Salimzadeh, S., Bakker, R., Nick, H., 2020. Experimental investigation of drilling lateral boreholes in chalk rocks with high-pressure jets. Int. J. Geomech. 20 (6), 04020049.
Mikelic, A., Wheeler, M., 2013. Convergence of iterative coupling for coupled flow and geomechanics. Comput. Geosci. 17 (3), 455–461.
Min, K., Rutqvist, J., Tsang, C., Jing, L., 2004. Stress-dependent permeability of fractured rock masses: A numerical study. Int. J. Rock Mech. Min. Sci. 41 (7), 1191–1210.
Morel, F., Hering, J., 1993. Principles and Applications of Aquatic Chemistry. John Wiley & Sons.
Mu, D., Liu, Z., Huang, C., Djilali, N., 2008. Determination of the effective diffusion coefficient in porous media including Knudsen effects. Microfluid. Nanofluid. 4 (3), 257–260.
Nejati, M., Dambly, M., Saar, M., 2019. A methodology to determine the elastic properties of anisotropic rocks from a single uniaxial compression test. J. Rock Mech. Geotech. Eng. 11 (6), 1166–1183.
Nick, H.M., Raoof, A., Centler, F., Thullner, M., Regnier, P., 2013. Reactive dispersive contaminant transport in coastal aquifers: Numerical simulation of a reactive henry problem. J. Contaminant Hydrol. 145, 90–104.
Nick, H.M., Schotting, R., Gutierrez-Neri, M., Johannsen, K., 2009. Modeling transverse dispersion and variable density flow in porous media. Transp. Porous Media 78 (1), 11–35.
Nick, H.M., Wolf, K. -H., Brhun, D., 2015. Mixed CO_2–water injection into geothermal reservoirs: A numerical study. In: Proceedings of World Geothermal Congress. pp. 19–25.
Onate, E., 1998. Derivation of stabilized equations for numerical solution of advective-diffusive transport and fluid flow problems. Comput. Methods Appl. Mech. Engrg. 151 (1–2), 233–265.
Pandey, S., Chaudhuri, A., 2017. The effect of heterogeneity on heat extraction and transmissivity evolution in a carbonate reservoir: A thermo-hydro-chemical study. Geothermics 69, 45–54.
Pandey, S., Chaudhuri, A., Kelkar, S., Sandeep, V., Rajaram, H., 2014. Investigation of permeability alteration of fractured limestone reservoir due to geothermal heat extraction using three-dimensional thermo-hydro-chemical (THC) model. Geothermics 51, 46–62.
Phillips, P., Wheeler, M., 2007a. A coupling of mixed and continuous Galerkin finite element methods for poroelasticity I: The continuous in time case. Comput. Geosci. 11 (2), 131.
Phillips, P., Wheeler, M., 2007b. A coupling of mixed and continuous Galerkin finite element methods for poroelasticity II: The discrete-in-time case. Comput. Geosci. 11 (2), 145–158.
Raoof, A., Nick, H.M., Hassanizadeh, S. Majid, Spiers, C.J., 2013. PoreFlow: A complex pore-network model for simulation of reactive transport in variably saturated porous media. Comput. Geosci. 61, 160–174.
Riviere, B., 2008. Discontinuous Galerkin Methods for Solving Elliptic and Parabolic Equations: Theory and Implementation. SIAM.
Riviere, B., Wheeler, M., 2000. A discontinuous Galerkin method applied to nonlinear parabolic equations. In: Discontinuous Galerkin Methods. Springer, pp. 231–244.
Rupp, A., Lee, S., 2020. Continuous Galerkin and enriched Galerkin methods with arbitrary order discontinuous trial functions for the elliptic and parabolic problems with jump conditions. J. Sci. Comput. 84, 9.
Rutqvist, J., 2017. An overview of TOUGH-based geomechanics models. Comput. Geosci. 108, 56–63.
Rutqvist, J., Stephansson, O., 2003. The role of hydromechanical coupling in fractured rock engineering. Hydrogeol. J. 11 (1), 7–40.
Rutqvist, J., Wu, Y., Tsang, C., Bodvarsson, G., 2002. A modeling approach for analysis of coupled multiphase fluid flow, heat transfer, and deformation in fractured porous rock. Int. J. Rock Mech. Min. Sci. 39 (4), 429–442.
Salimzadeh, S., Hagerup, E., Kadeethum, T., Nick, H., 2019. The effect of stress distribution on the shape and direction of hydraulic fractures in layered media. Eng. Fract. Mech. 215, 151–163.
Salimzadeh, S., Nick, H., 2019. A coupled model for reactive flow through deformable fractures in enhanced geothermal systems. Geothermics 81, 88–100.
Scovazzi, G., Wheeler, M., Mikelic, A., Lee, S., 2017. Analytical and variational numerical methods for unstable miscible displacement flows in porous media. J. Comput. Phys. 335, 444–496.
Sun, S., Liu, J., 2009. A locally conservative finite element method based on piecewise constant enrichment of the continuous Galerkin method. SIAM J. Sci. Comput. 31 (4), 2528–2548.
Taheriotaghsara, M., Bonto, M., Eftekhari, A., Nick, H., 2020. Prediction of oil breakthrough time in modified salinity water flooding in carbonate cores. Fuel 274, 117806.
Tjaden, B., Cooper, S., Brett, D., Kramer, D., Shearing, P., 2016. On the origin and application of the Bruggeman correlation for analysing transport phenomena in electrochemical systems. Curr. Opin. Chem. Eng. 12, 44–51.
Tran, M., Jha, B., 2020. Coupling between transport and geomechanics affects spreading and mixing during viscous fingering in deformable aquifers. Adv. Water Resour. 136, 103485.
Vik, H., Salimzadeh, S., Nick, H., 2018. Heat recovery from multiple-fracture enhanced geothermal systems: The effect of thermoelastic fracture interactions. Renew. Energy.
Yortsos, Y., Salin, D., 2006. On the selection principle for viscous fingering in porous media. J. Fluid Mech. 557, 225–236.
Zhang, C., Zarrouk, S., Archer, R., 2016. A mixed finite element solver for natural convection in porous media using automated solution techniques. Comput. Geosci. 96, 181–192.
Zhao, Y., Choo, J., 2020. Stabilized material point methods for coupled large deformation and fluid flow in porous materials. Comput. Methods Appl. Mech. Engrg. 362, 112742.